

A Gibbs Energy Minimization Approach for Modeling of Chemical Reactions in a Basic Oxygen Furnace

Ari Kruskopf^{1)*} and Ville-Valtteri Visuri²⁾

1) Research Group for Materials Processing and Powder Metallurgy

Department of Chemical and Metallurgical Engineering

Aalto University

PO Box 16200

Vuorimiehentie 2, Espoo

FI-00076 Aalto, Finland

2) Process Metallurgy Research Unit

University of Oulu

PO Box 4300

FI-90014 University of Oulu, Finland.

*) Corresponding author. E-mail: ari.kruskopf@aalto.fi

19 **Abstract**

20 In modern steelmaking, the decarburisation of hot metal is converted into steel primarily in
21 converter processes, such as the basic oxygen furnace (BOF). The objective of this work was to
22 develop a new mathematical model for top blown steel converter, which accounts for the complex
23 reaction equilibria in the impact zone, also known as the hot spot, as well as the associated mass and
24 heat transport. An in-house computer code of the model has been developed in Matlab. The main
25 assumption of the model is that all the reactions take place in a specified reaction zone. The mass
26 transfer between the reaction volume, bulk slag and metal determine the reaction rates for the
27 species. The thermodynamic equilibrium is calculated using the partitioning of Gibbs energy (PGE)
28 method. The activity model for the liquid metal is the unified interaction parameter (UIP) model
29 and for the liquid slag the modified quasichemical model (MQM). The MQM was validated by
30 calculating iso-activity lines for the liquid slag components. The PGE method together with the
31 MQM was validated by calculating liquidus lines for solid components. The results were compared
32 with measurements from literature. The full chemical reaction model was validated by comparing
33 the metal and slag compositions to measurements from industrial scale converter. The predictions
34 were found to be in good agreement with the measured values. Furthermore, the accuracy of the
35 model was found to compare favourably with the models proposed in the literature. The real time
36 capability of the proposed model was confirmed in test calculations.

37
38 **Keywords:** steelmaking, basic oxygen furnace, mathematical modelling, thermodynamic
39 equilibrium.

40

41

1 Introduction

In modern steelmaking, the decarburisation of hot metal is converted into steel primarily in converter processes, such as the basic oxygen furnace (BOF). The BOF process is characterised by a high oxygen supply rate through a supersonic top lance and by the resulting high rate of decarburisation. The most common type of such processes is the Linz-Donawitz converter, *i.e.* the Basic Oxygen Furnace, and its numerous variants. During the BOF process, the carbon content of the metal bath decreases from approximately 4–4.5 wt-% to 0.02–1 wt-%, depending on the final carbon target, while the temperature of the metal bath increases from 1473–1573 K (1200–1300 °C) to 1873–1973 K (1600–1700 °C) due to exothermic oxidation reactions.³⁷

1.1 Dynamics of the BOF process

The interaction of the gas jet with metal bath is a complex phenomenon^{1 2 3}. The momentum of the gas jet induces a cavity, which is in continuous oscillating motion. The quasi-steady state geometry of the cavity surface can be described as a paraboloid of revolution.⁴ The behaviour of the cavity can be categorised into dimpling, splashing and penetrating modes.¹ If the shear force at the interface becomes sufficiently large, metal droplets are detached from the edges of the cavity. For a given cavity mode, the amount of metal droplets generated increases as a function of the so-called *blowing number*, a dimensionless property which describes the ratio of gas jet inertia to surface tension forces of the metal bath.^{5 6} The size distribution of the metal droplets can be described using the Rosin-Rammler-Sperling distribution.^{7 8} Through their vast interfacial area, the metal droplets play an important role in the decarburisation⁹ and dephosphorisation¹⁰ reactions.

A large body of experimental literature^{9,11,12,13,14,15} has been dedicated to the kinetics of the BOF process. With the help of the knowledge obtained, a considerable progress has been made in the mathematical description of individual aspects of the process. Nowadays, the greatly increased computational resources permit both detailed mathematical^{16,17,18,19,20,21,22,23,24,25,26} and data-driven

models^{27,28,29,30,31}. The former type of models aim to account for all the dominating mechanisms and phenomena and to provide insight on the dynamics of the process, while the latter type of models aim to provide accurate predictions based on statistical analysis of measurement information.

The main aspects to be covered by the mathematical models are the dynamics of decarburization reaction and the accompanying oxidation reactions of species in the metal bath and their effect on the evolution of the composition and temperature of the metal and slag phases. The dynamics of decarburization in the BOF process are characterized by three distinctive periods: “start”, “linear decline” and “phasing out”.^{32,33} In the early part of refining, most of the oxygen injected is consumed for oxidation of minor elements, such as Si, Mn, P, Ti and V, and therefore the decarburization rate is low.^{34,35,36,37} In the subsequent period the carbon content decreases linearly and the decarburization rate is controlled by oxygen supply.^{32,33} When a critical value of carbon content reached, the mass transfer of dissolved carbon becomes the rate-limiting step and the decarburisation rate starts to decrease linearly as a function of the carbon content.^{32,33} Because carbon is no longer able to reduce all the FeO formed, the FeO content of the slag starts to increase rapidly.^{19,25,33,34,36,37} A characteristic feature of the dynamics of the BOF process is the partial reduction of oxidized P and Mn back to the metal bath during the period of “linear decline” and subsequent oxidation in the period of “phasing out”.^{19,25,34,36,37} The description of the dynamics of the process is complicated further by melting of scrap and dissolution of slag formers.

1.2 Mathematical modelling of the BOF process

Mathematical models, which are the primary interest of this work, are indispensable in designing of new production and operating practices without *a priori* experimental data. Dynamic mathematical models can be divided loosely into two main categories: *reaction interface models* and *reaction volume models*. The reaction interface models make use of the boundary layer approach and assume that the overall reaction rates are controlled by the mass transfer resistance in the diffusion

boundary layers. For example, in the case of a non-emulsified system with permanent phase contact, the rate expression of species i then expressed according to a first-order scheme:

$$\frac{dm_i}{dt} = -h_Y A \rho (y_i - y_i^*), \quad (1)$$

where y denotes the mass fraction, h_Y is the mass transfer coefficient, A is the interfacial area, ρ is the density volume, and y^* is the interfacial mass fraction. While the reaction interface models offer interesting information on the microkinetic behavior of reaction systems, the main difficulty associated with such models is the very definition of the reaction interfaces and mass transport coefficients that govern the overall rate. Further complexity is induced by the treatment of parallel mass transfer limited reactions; an exhaustive discussion on the available approaches has been presented in earlier work³⁸. Numerous examples on the application of the reaction interface approach for modelling of the BOF process are available in the literature^{16,17,18,19,20,21,22,23,24,25,26}.

The reaction volume models, on the other hand, focus on mass exchange between passive bulk volumes and active reaction volumes, which are assumed to reach their thermodynamic equilibrium composition at every instant. The rate expression corresponding to Eq. 1 can be expressed as follows:

$$\frac{dm_i}{dt} = -\dot{m}_{in} y_{i,in} + \dot{m}_{i,out} y_{i,out}, \quad (2)$$

where \dot{m}_{in} and \dot{m}_{out} denote the mass fluxes into and from the reaction volume, respectively. The reaction equilibrium model approach is in many ways analogous to the control volume methods employed in computational fluid dynamics. On the other hand, the reaction equilibrium approach is naturally compatible with computational thermodynamics software. So far, there have already been

115 successful attempts^{39,40} to couple computational fluid dynamics with thermodynamic software in
116 the context of basic oxygen steelmaking. A practical limitation of such models, however, is their
117 relatively high computational expense, even in the case of a pre-calculated or time-averaged fluid
118 flow field. Therefore, more research is required in order to derive models, which provide detailed
119 information, but are sufficiently fast for industrial applications.

120 1.3 Objectives of this work

121 In earlier work, mathematical models were developed for scrap melting^{41,42} and bottom stirring⁴³ in
122 the BOF process. The objective of this work was to develop a detailed mathematical model, which
123 accounts for the complex reaction equilibria in the impact zone, also known as the *hot spot*, as well
124 as the associated mass and heat transport. Because of the complicated phenomena present in the
125 process, it is important to validate the different areas of physics separately so that the final model
126 could be as reliable as possible. The aim of this model is to achieve real time calculation of the
127 actual process using a desktop computer. In this work, a chemical reaction part of the process model
128 is developed and validated using plant data from an industrial scale BOF converter. The chemical
129 reactions are modeled using in-house program for the determination of thermodynamic equilibrium.
130 A program code was developed during this work in Matlab for the full chemical reaction model.
131 The thermodynamic equilibrium is calculated for the reaction zone and for the bulk slag phase.
132 Mass transfer from the bulk phases determines the reaction zone mass and volume. The novelty of
133 the model lies in the fast, yet detailed calculation of reaction equilibria in the BOF process. The
134 thermodynamic equilibrium method provides the possibility of predicting the solidification of
135 components in the slag and it also automatically takes into account simultaneous reactions taking
136 place in the converter.

137 2 Algorithm for Gibbs Energy Minimization

138 An in-house Matlab code was developed for the computation of the thermodynamic equilibrium in
 139 this work. The algorithm used for Gibbs energy minimization is the Partitioning of Gibbs energy
 140 (PGE) method^{44,45}. The starting point for the method is the definition of the chemical potentials of
 141 all species and phases by the chemical potentials of the system components. The Gibbs free energy
 142 is then divided among the system components in a way that progressively reduces the residuals of
 143 the mass balance equations. A brief description of the method is provided in the following. The
 144 integral Gibbs free energy of a multicomponent multiphase system G is expressed by

$$\frac{G}{RT} = \sum_{l=1}^L n_l \sum_{i=1}^{N_l} x_{i(l)} \mu_i + \sum_{k=1}^K n_k \mu_k, \quad (3)$$

145 where R is the universal gas constant, T is the absolute temperature, L is the number of solution
 146 phases, K is the number of pure phases and N_l is the number of constituents in a phase l . The
 147 number of moles and the molar fraction of component i in phase l are denoted by n_l and $x_{i(l)}$,
 148 respectively. The dimensionless chemical potentials of a constituent i in a solution phase l and pure
 149 phase k are μ_i and μ_k , respectively. The dimensionless chemical potential of a pure phase in a
 150 standard state is $g_{i(l)}^\circ$. The dimensionless chemical potential of an ideal phase is

$$\mu_i = \frac{\tilde{\mu}_i}{RT} = g_{i(l)}^\circ + \ln(x_{i(l)}), \quad (4)$$

151 where the second term on the right hand side is the dimensionless entropy of ideal mixing and $\tilde{\mu}_i$ is
 152 the dimensional chemical potential. To account for the non-ideal behaviour of species the excess
 153 Gibbs energy $g_{i(l)}^{\text{ex}}$ is added to the chemical potential:

$$\mu_i = \frac{\tilde{\mu}_i}{RT} = g_{i(l)}^\circ + \ln(x_{i(l)}) + g_{i(l)}^{\text{ex}}, \quad (5)$$

154 The thermodynamic equilibrium must be subjected to the mass balance constraints

$$b_j = \sum_{l=1}^L n_l \sum_{i=1}^{N_l} x_{i(l)} a_{ij} + \sum_{k=1}^K n_k a_{kj}, \quad (6)$$

155 where a_{ij} and a_{kj} are stoichiometry matrices containing the coefficients for the species and system
 156 components j . The sum of mole fractions of all constituents in a solution phase l is

$$x_L = \sum_{i=1}^{N_L} x_{i(l)}, \quad (7)$$

157 which at convergence must be equal to one. The thermodynamic equilibrium must also be subjected
 158 to the Gibbs phase rule

$$F = C - \Phi + 2, \quad (8)$$

159 where F is the number of degrees of freedom, C is the number of components and $\Phi = (L + K)$, is
 160 the number of phases. In the chemical reaction model during time-integration pressure and
 161 temperature have a singular value at each time step. This means that for every converged result at
 162 every time-step the computed thermodynamic equilibrium is considered as isothermal and isobaric
 163 system. The Gibbs phase rule is then

$$F = C - \Phi, \quad (9)$$

164 which means that the number of stable phases cannot exceed the number of components. The final
 165 condition for equilibrium is that global minimum has been found for the system Gibbs energy. In
 166 other words the chemical potentials of the system components Γ_j multiplied by the stoichiometric
 167 coefficients a_{ij} and summed together must equal the constituent chemical potentials:

$$\mu_i = \sum_{j=1}^C a_{ij} \Gamma_j. \quad (10)$$

168 In the PGE method Eqs. (5) and (10) are set to be equal. Then the mole fractions are solved
 169 according to

$$x_{i(l)} = \exp \left(\sum_{j=1}^C a_{ij} \Gamma_j - g_{i(l)}^\circ - g_{i(l)}^{ex} \right), \quad (11)$$

170 and they are substituted into the mass balances

$$b_j = \sum_{l=1}^L n_l \sum_{i=1}^{N_l} \exp \left(\sum_{j=1}^C a_{ij} \Gamma_j - g_{i(l)}^{\circ} - g_{i(l)}^{ex} \right) a_{ij} + \sum_{k=1}^K n_k a_{kj}, \quad (12)$$

171 which are now dependent on the component potentials Γ_j . The system of equations to be solved
 172 consists of Eqs. (7), (10) and (12). These equations are solved using Newton-Raphson method and
 173 thus they are reorganized to be equal to zero:

$$\begin{aligned} f_v &= \sum_{l=1}^L n_l^s \sum_{i=1}^{N_l} \exp \left(\sum_{j=1}^C a_{ij} \Gamma_j - g_{i(l)}^{\circ} - g_{i(l)}^{ex} \right) a_{iv} + \sum_{k=1}^K n_k^p a_{kj} - b_j = 0, \\ h_l &= \sum_{i=1}^{N_l} \exp \left(\sum_{j=1}^C a_{ij} \Gamma_j - g_{i(l)}^{\circ} - g_{i(l)}^{ex} \right) - 1 = 0, \\ q_k &= \sum_{j=1}^C a_{kj} \Gamma_j - \mu_k = \sum_{j=1}^C a_{kj} \Gamma_j - g_k^0 = 0, \end{aligned} \quad (13)$$

174 The h_l equations cover the solution phases and the q_k equations the pure phases, hence $\mu_k = g_k^{\circ}$.
 175 The number of equations in the system is $C + L + K$. When Newton-Raphson is applied, the system
 176 of non-linear equations becomes

$$\begin{aligned} J dx_j &= \frac{\partial F_i}{\partial x_j} dx_j = -F_i, \\ F_i &= (f_1, \dots, f_C, h_1, \dots, h_L, q_1, \dots, q_K), \\ dx_j &= (d\Gamma_1, \dots, d\Gamma_C, dn_1^s, \dots, dn_L^s, dn_1^p, \dots, dn_K^p), \end{aligned} \quad (14)$$

177 where J is the Jacobian matrix, while superscripts p and s denote pure and solution, respectively.
 178 The Jacobian matrix

$$J = \begin{pmatrix} \frac{\partial f_v}{\partial \Gamma_j} & \frac{\partial f_v}{\partial n_l^s} & \frac{\partial f_v}{\partial n_k^p} \\ \frac{\partial h_l}{\partial \Gamma_j} & \frac{\partial h_l}{\partial n_l^s} & \frac{\partial h_l}{\partial n_k^p} \\ \frac{\partial q_k}{\partial \Gamma_j} & \frac{\partial q_k}{\partial n_l^s} & \frac{\partial q_k}{\partial n_k^p} \end{pmatrix} = \begin{pmatrix} \sum_{l=1}^L n_l \sum_{i=1}^{N_l} a_{ij} a_{iv} x_{i(l)} & \sum_{i=1}^{N_l} a_{iv} x_{i(l)} & a_{kj} \\ \sum_{i=1}^{N_l} a_{ij} x_{i(l)} & 0 & 0 \\ a_{kj} & 0 & 0 \end{pmatrix}, \quad (15)$$

179 is symmetric. The system is solved for dx_j and the solution is updated

$$x_j^{v+1} = x_j^v + \alpha dx_j, \quad (16)$$

180 where α is an under-relaxation factor. The problem is determined by the mass constraints b_j and

181 temperature. In the current algorithm in this work the problem is scaled as follows:

$$b_j^* = \frac{b_j}{\sum_{k=1}^C b_k}, \quad (17)$$

182 which means the sum of b_j^* always equals one. The factor α is chosen such that the maximal change
 183 for phase mole amount in single iteration can be only 10% of the maximal value that the phase can
 184 contain. Factors for all phases are calculated from

$$\alpha_j = \min\left(\frac{0.1n_j^{\max}}{dn_j}, 1\right), \quad (18)$$

185 and the smallest factor is chosen from α_j for all variables in Eq. (16). n_j^{\max} is calculated by
 186 assuming all possible components in b_j are in the particular phase. This is an estimate for the
 187 maximal molar amount for the particular phase. The PGE method requires good initial values at the
 188 start of the iterations; these can be generated using the Leveling and Post-Leveling methods⁴⁶.

189

190 During the course of iterations, a phase can have a negative molar amount. At convergence this
 191 means that the phase is unstable and should be removed from the stable phase collection. A pure
 192 phase is added to the phase collection if its driving force

$$D = g_i^\circ - \sum_{j=1}^C a_{ij}\Gamma_j, \quad (19)$$

193 is negative. A solution phase is added to the collection if the sum of hypothetical molar amounts of
 194 the phase l is equal or greater than one:

$$x_L = \sum_{i=1}^{N_l} x_{i(l)} = \sum_{i=1}^{N_l} \exp\left(\sum_{j=1}^C a_{ij}\Gamma_j - g_{i(l)}^\circ - g_{i(l)}^{\text{ex}}\right), \quad (20)$$

195 In the current model, only one phase can be removed or added at the same time. For the current
 196 problem, this approach satisfies the Gibbs phase rule automatically. If more phases are added or
 197 removed simultaneously, the stability of the PGE algorithm weakens.

198

199 Since the sum of the mole fractions of the solution phases can be far from unity during iterations,

200 the update of the excess Gibbs energies for the non-ideal phases is not conducted in every iteration.
201 As a rule, the excess Gibbs energies are calculated only if the sum of the mole fractions is less than
202 1.001. This is important especially in the case of the quasichemical activity model, which assumes
203 that the sum of the molar fractions is equal to one. When new values $g_{i(l)}^*$ for excess Gibbs free
204 energies are calculated, the values used in the PGE algorithm are updated with

$$g_{i(l)}^{\nu+1} = g_{i(l)}^{\nu} + \alpha(g_{i(l)}^* - g_{i(l)}^{\nu}), \quad (21)$$

205 where the update is under-relaxed. This type of under-relaxation is important to achieve stability
206 and convergence for PGE.

207

208 3 Activity Models

209 The steel converter application contains two non-ideal phases. These are the slag and the steel
210 phases. The activity model for the steel phase is the unified interaction parameter (UIP)
211 formalism⁴⁷. The modified quasichemical model (MQM) was applied to calculate activities of slag
212 components.

213 3.1 Activity of species in the metal phase

214 In the UIP formalism, the temperature dependent molar first-order parameters from Sigworth⁴⁸ are
215 used unless otherwise mentioned. The excess Gibbs energy can be calculated for element i from

$$\frac{g_i^{\text{ex}}}{RT} = \ln(\gamma_i) = \ln(\gamma_i^{\circ}) + \ln(\gamma_{\text{solvent}}) + \sum_j \varepsilon_{ij} X_j = g_i^{\text{sl}} + \ln(\gamma_{\text{solvent}}) + \sum_j \varepsilon_{ij} X_j, \quad (22)$$

216 where ε denote the molar first-order interaction parameters. Here, the solvent is iron and the sum
217 term loops over every element except iron. The solvent activity coefficient can be calculated from

$$\ln(\gamma_{\text{solvent}}) = -\frac{1}{2} \sum_k \sum_j \varepsilon_{jk} X_j X_k. \quad (23)$$

218 For the oxygen interaction parameter $\varepsilon_{O,O}$ a fit was made to match the activity model of Miettinen⁴⁹.

219 The interaction parameter is a linear function of temperature as follows:

$$\varepsilon = A + B/T \quad (24)$$

220 In the case of oxygen the coefficients $A = 100$ and $B = -115400$ are used. Coefficients
221 $A = -46.8$ and $B = 107000$ are used for the C-Si interaction parameter below $T = 1627^{\circ}\text{C}$
222 (1900 K). The rest of the parameters can be found from Table 1.

223

224 3.2 Activities of species in the slag phase

225 The modified quasichemical model for ternary case is employed for the slag phase. In the
226 quasichemical approach, the atoms of molecules of a solution are distributed over the sites of a
227 quasi lattice. In the pair approximation pair exchange reactions are considered as follows:

$$(q - q) + (w - w) = 2(q - w), \quad \Delta g_{qw} \quad (25)$$

where q and w represent the nearest neighbour pairs. The nonconfigurational Gibbs energy change for the formation of two moles of $(q - w)$ pairs is Δg_{qw} . The molar amounts of components n_q and pairs n_{qw} are connected according to

$$Z_q n_q = 2n_{qw} + \sum_{q \neq w} n_{qw}, \quad (26)$$

where Z_q is the coordination number of component q . Pair fractions X_{qw} , mole fractions X_q and coordination equivalent fractions Y_q are as follows:

$$X_{qw} = \frac{n_{qw}}{\sum n_{ij}}, \quad X_q = \frac{n_q}{\sum n_i}, \quad Y_q = \frac{Z_q n_q}{\sum Z_i n_i}, \quad (27)$$

The Gibbs energy of solution in the ternary case (A,B,C) is

$$G = n_A g_A^\circ + n_B g_B^\circ + n_C g_C^\circ - T \Delta S^{\text{config}} + n_{AB} \frac{\Delta g_{AB}}{2} + n_{AC} \frac{\Delta g_{AC}}{2} + n_{BC} \frac{\Delta g_{BC}}{2}, \quad (28)$$

where the configurational entropy of mixing is approximately as follows:

$$-\frac{\Delta S^{\text{config}}}{R} = n_A \ln(X_A) + n_B \ln(X_B) + n_C \ln(X_C) + n_{AA} \ln\left(\frac{X_{AA}}{Y_A^2}\right) + n_{BB} \ln\left(\frac{X_{BB}}{Y_B^2}\right) + n_{CC} \ln\left(\frac{X_{CC}}{Y_C^2}\right) \\ + n_{AB} \ln\left(\frac{X_{AB}}{2Y_A Y_B}\right) + n_{AC} \ln\left(\frac{X_{AC}}{2Y_A Y_C}\right) + n_{BC} \ln\left(\frac{X_{BC}}{2Y_B Y_C}\right) \quad (29)$$

For the binary system (A-B) the pair Gibbs energy is expanded as an empirical polynomial in the component fractions

$$\Delta g_{AB} = \Delta g_{AB}^\circ + \sum_{i+j \geq 1} q_{AB}^{ij} Y_A^i Y_B^j, \quad (30)$$

where the empirical coefficients q_{AB}^{ij} are in the general case functions of temperature

$$q_{AB}^{ij} = \omega_{AB}^{ij} - \eta_{AB}^{ij} T \quad (31)$$

The chemical potentials for components (A,B,C) can be derivated from Eq. (28) as follows:

$$\mu_A = \frac{Z_A}{2} \left(\frac{\partial G}{\partial n_{AA}} \right) = g_A^\circ + RT \ln(X_A) + Z_A RT \ln\left(\frac{X_{AA}}{Y_A^2}\right) + \frac{Z_A}{2} \frac{\partial}{\partial n_{AA}} (n_{AB} \Delta g_{AB} + n_{BC} \Delta g_{BC} + n_{AC} \Delta g_{AC}) \\ \mu_B = \frac{Z_B}{2} \left(\frac{\partial G}{\partial n_{BB}} \right) = g_B^\circ + RT \ln(X_B) + Z_B RT \ln\left(\frac{X_{BB}}{Y_B^2}\right) + \frac{Z_B}{2} \frac{\partial}{\partial n_{BB}} (n_{AB} \Delta g_{AB} + n_{BC} \Delta g_{BC} + n_{AC} \Delta g_{AC}) \\ \mu_C = \frac{Z_C}{2} \left(\frac{\partial G}{\partial n_{CC}} \right) = g_C^\circ + RT \ln(X_C) + Z_C RT \ln\left(\frac{X_{CC}}{Y_C^2}\right) + \frac{Z_C}{2} \frac{\partial}{\partial n_{CC}} (n_{AB} \Delta g_{AB} + n_{BC} \Delta g_{BC} + n_{AC} \Delta g_{AC}) \quad (32)$$

239 The derivatives of the pair Gibbs energies depend on the exact polynomial approximations used and
 240 the interpolation method used to approximate the binary energies in the ternary system. The ternary
 241 system in this work is CaO-SiO₂-FeO system. The pair Gibbs free energies for the binaries are as
 242 follows⁵⁰:

$$\begin{aligned}\Delta g_{\text{CaO-SiO}_2} &= (-185912 + 25.104T) - 72814.2Y_{\text{SiO}_2}^3 + (213710.4 - 41.84T)Y_{\text{SiO}_2}^6, \\ \Delta g_{\text{FeO-SiO}_2} &= (13886.7) + (-86889.1 + 29.29T)Y_{\text{SiO}_2} + 951483.4Y_{\text{SiO}_2}^5 - 1786346Y_{\text{SiO}_2}^6 \quad (33) \\ &\quad + (1086614 - 62.76T)Y_{\text{SiO}_2}^7, \\ \Delta g_{\text{CaO-FeO}} &= -26447.1 - 18756.9Y_{\text{FeO}},\end{aligned}$$

243 where the accompanying coordination numbers are $Z_{\text{SiO}_2} = 1.3774$, $Z_{\text{CaO}} = Z_{\text{FeO}} = 0.6887$. The
 244 binary Gibbs free energies are interpolated to the ternary system using the asymmetric
 245 approximation called the Kohler-Toop method. In the asymmetric approximation, one of the three
 246 components is considered asymmetric. Since SiO₂ is acidic and the two other components are basic,
 247 the SiO₂ component is considered as asymmetric in this work. After the asymmetric interpolation
 248 the Gibbs energies are

$$\begin{aligned}\Delta g_{\text{CaO-SiO}_2} &= (-185912 + 25.104T) - 72814.2Y_{\text{SiO}_2}^3 + (213710.4 - 41.84T)Y_{\text{SiO}_2}^6, \\ \Delta g_{\text{FeO-SiO}_2} &= (13886.7) + (-86889.1 + 29.29T)Y_{\text{SiO}_2} + 951483.4Y_{\text{SiO}_2}^5 - 1786346Y_{\text{SiO}_2}^6, \\ &\quad + (1086614 - 62.76T)Y_{\text{SiO}_2}^7 \quad (34) \\ \Delta g_{\text{CaO-FeO}} &= -26447.1 - 18756.9 \frac{Y_{\text{FeO}}}{Y_{\text{FeO}} + Y_{\text{CaO}}},\end{aligned}$$

249 Now that the Gibbs energies for binary pairs are known in the ternary system, the derivatives in the
 250 chemical potentials of the components can be computed:

$$\begin{aligned}\frac{Z_A}{2} \frac{\partial}{\partial n_{AA}} (n_{AB}\Delta g_{AB} + n_{BC}\Delta g_{BC} + n_{AC}\Delta g_{AC}) &= -\frac{Z_A}{2} \left[Y_B \left(X_{AB} \frac{\partial \Delta g_{AB}}{\partial Y_B} + X_{BC} \frac{\partial \Delta g_{BC}}{\partial Y_B} \right) + X_{AC} \frac{Y_C}{(Y_A + Y_C)^2} \frac{\partial \Delta g_{AC}}{\partial Y_C / (Y_A + Y_C)} \right], \\ \frac{Z_B}{2} \frac{\partial}{\partial n_{BB}} (n_{AB}\Delta g_{AB} + n_{BC}\Delta g_{BC} + n_{AC}\Delta g_{AC}) &= \frac{Z_B}{2} (1 - Y_B) \left(X_{AB} \frac{\partial \Delta g_{AB}}{\partial Y_B} + X_{BC} \frac{\partial \Delta g_{BC}}{\partial Y_B} \right), \\ \frac{Z_C}{2} \frac{\partial}{\partial n_{CC}} (n_{AB}\Delta g_{AB} + n_{BC}\Delta g_{BC} + n_{AC}\Delta g_{AC}) &= \frac{Z_C}{2} \left[-Y_B \left(X_{AB} \frac{\partial \Delta g_{AB}}{\partial Y_B} + X_{BC} \frac{\partial \Delta g_{BC}}{\partial Y_B} \right) + X_{AC} \frac{Y_A}{(Y_A + Y_C)^2} \frac{\partial \Delta g_{AC}}{\partial Y_C / (Y_A + Y_C)} \right],\end{aligned} \quad (35)$$

251 where $A = \text{CaO}$, $B = \text{SiO}_2$ and $C = \text{FeO}$.

252 3.2.1 Equation system for pair fractions

253 The six pair fractions ($X_{AA}, X_{BB}, X_{CC}, X_{AB}, X_{AC}, X_{BC}$) in Eqs. (32) and (35) have to be solved separately

254 using an iterative algorithm. First equations for pair fractions have to be formed. This can be done
 255 by minimizing the solution Gibbs energy algebraically at constant composition ($n_A, n_B, n_C =$
 256 $const.$). The three equations

$$\begin{aligned}\frac{X_{AB}^2}{X_{AA}X_{BB}} &= 4 \exp\left(\frac{-\Delta g_{AB}}{RT}\right), \\ \frac{X_{BC}^2}{X_{BB}X_{CC}} &= 4 \exp\left(\frac{-\Delta g_{BC}}{RT}\right), \\ \frac{X_{AC}^2}{X_{AA}X_{CC}} &= 4 \exp\left(\frac{-\Delta g_{AC}}{RT}\right),\end{aligned}\tag{36}$$

257 can be obtained by derivating the solution Gibbs energy, Eq. (28), with respect to n_{AB} , n_{BC} and n_{AC} ,
 258 respectively and by setting the derivatives equal to zero. Additional three equations

$$\begin{aligned}X_{AA} &= Y_A - \frac{X_{AB} + X_{AC}}{2}, \\ X_{BB} &= Y_B - \frac{X_{AB} + X_{BC}}{2}, \\ X_{CC} &= Y_C - \frac{X_{AC} + X_{BC}}{2},\end{aligned}\tag{37}$$

259 can be formed using Eqs. (26) and (27).

260 3.2.2 Iterative Newton-Raphson algorithm for pair fractions

261 Newton-Raphson algorithm is used for the solution of the pair fraction equations, which require a
 262 simultaneous solution. First Eqs. (36) are reorganised into Eq. (38).

$$\begin{aligned}X_{AB} - 2\sqrt{K_{AB}^{-1}X_{AA}X_{BB}} &= 0, \\ X_{BC} - 2\sqrt{K_{BC}^{-1}X_{BB}X_{CC}} &= 0, \\ X_{AC} - 2\sqrt{K_{AC}^{-1}X_{AA}X_{CC}} &= 0,\end{aligned}\tag{38}$$

263 Some of the mathematical solutions to the pair fraction equations contain values outside of the
 264 permitted range [0,1]. Negative solutions can be avoided by changing of variables. One of the ways
 265 this can be achieved is by making a substitution $Z^2 = X$ for all pair fractions. Now the Z variables
 266 can have negative solutions, but the real pair fractions X will have only positive values. By
 267 summing Eqs. (37) and invoking $Y_A + Y_B + Y_C = 1$, it can be seen that the sum of all pair fractions

268 equal unity. This means that if the negative solutions can be avoided, automatically greater than one
 269 values can be avoided at the same time. The final system of equations for Newton-Raphson
 270 algorithm is

$$\begin{aligned}
 f_1 &= Z_{AB}^2 - 2Z_{AA}Z_{BB}K_{AB}^{-1/2} = 0, \\
 f_2 &= Z_{BC}^2 - 2Z_{BB}Z_{CC}K_{BC}^{-1/2} = 0, \\
 f_3 &= Z_{AC}^2 - 2Z_{AA}Z_{CC}K_{AC}^{-1/2} = 0, \\
 f_4 &= Z_{AA}^2 - Y_A + \frac{1}{2}(Z_{AB}^2 + Z_{AC}^2) = 0, \\
 f_5 &= Z_{BB}^2 - Y_B + \frac{1}{2}(Z_{AB}^2 + Z_{BC}^2) = 0, \\
 f_6 &= Z_{CC}^2 - Y_C + \frac{1}{2}(Z_{AC}^2 + Z_{BC}^2) = 0,
 \end{aligned} \tag{39}$$

271 The system $J\Delta Z = -f$ is solved and the solution is updated with Eq. (16). After the solution has
 272 converged the pair fraction values can be calculated using substitution $X = Z^2$. More about
 273 generating a good quality initial value for the method can be found from the Appendix 1.

274

275 **4 Description of the BOF model**

276 The steel converter model contains three main bulk phases, which are gas, slag and metal. Inert
277 bottom gas stirring mixes the liquid metal, while the top lance provides the oxygen required by the
278 refining reactions. Furthermore, the top lance contributes to the mixing of slag phase. The mass
279 from the bulk phases flow to the interfacial area between them. Here is a list of the main
280 assumptions in the model:

- 281 • a single reaction zone for all reactions
- 282 • three main bulk phases, gas (ideal), liquid slag (MQM activity), liquid metal (UIP activity)
- 283 • gas phase components: O_2 , CO , CO_2
- 284 • metal phase components: Fe, C, Si
- 285 • slag phase components: SiO_2 , CaO , FeO
- 286 • all mass in the reaction zone reaches thermodynamic equilibrium
- 287 • mass transfer between the bulk phases and the reaction zone determines the evolution of the
288 reactions
- 289 • constant pressure 1 atm at the reaction zone
- 290 • top lance gas jet affect only the mass transfer between the bulk slag and the reaction zone
- 291 • bottom gas stirring affects only the mass transfer between the bulk metal and the reaction
292 zone
- 293 • constant heat and mass transfer coefficients between the scrap and the bulk metal
- 294 • no heat transfer between the melt and the furnace lining
- 295 • no heat transfer between the gas injected from the furnace bottom and the metal phase

296 **4.1 Reaction zone**

297 The volume close to the interfaces is called a reaction zone. The mass inside the reaction zone is
298 assumed to reach a thermodynamic equilibrium at any instant. The phases at the equilibrium flow

299 from the reaction zone back into the respective bulk phases. The mass transfer parameters between
 300 the bulk phases and the reaction zone determine the amount of mass and energy that is transported
 301 into the reaction zone. The mass fluxes from the bulk phases are

$$\dot{m}_m = \rho_m \dot{V}_m, \quad \dot{m}_s = \rho_s \dot{V}_s, \quad \dot{m}_g = \rho_{O_2} \dot{V}_{O_2}, \quad (40)$$

302 where ρ is the density and \dot{V} is the volume flux. Subscripts m , s and g denote metal, slag and gas,
 303 respectively. The volume fluxes contain empirical functions. The total mass flux to the reaction
 304 zone is

$$\dot{m}_{RZ} = \dot{m}_m + \dot{m}_s + \dot{m}_g, \quad (41)$$

305 and the corresponding equilibrium mass fluxes are

$$\dot{m}_{RZ}^e = \dot{m}_m^e + \dot{m}_s^e + \dot{m}_g^e, \quad (42)$$

306 The heat fluxes transported from the bulk phases into the reaction zone are

$$\dot{H}_{RZ} = \dot{H}_m + \dot{H}_s + \dot{H}_g = \dot{m}_m h_m + \dot{m}_s h_s + \dot{m}_g h_g, \quad (43)$$

307 where h is the specific enthalpy. The total energy before and after equilibrium must be equal. The
 308 equilibrium enthalpies are

$$\dot{H}_{RZ}^e = \dot{H}_m^e + \dot{H}_s^e + \dot{H}_g^e, \quad (44)$$

309

310 Since the equilibrium temperature at the reaction zone is not known a priori initially the equilibrium
 311 temperature has to be guessed. Because the equilibrium enthalpy is not yet matching the initial
 312 enthalpy there exists an enthalpy difference between them:

$$\dot{H}_{RZ}^e - \dot{H}_{RZ} = \dot{H}_m^e + \dot{H}_s^e + \dot{H}_g^e - \dot{H}_{RZ} = \Delta \dot{H}_{RZ}, \quad (45)$$

313 To make the enthalpies equal the specific heat capacity functions c_p of the phases are integrated
 314 with

$$\dot{m}_m^e c_{p,m} \Delta T + \dot{m}_s^e c_{p,s} \Delta T + \dot{m}_g^e c_{p,g} \Delta T = -\Delta \dot{H}_{RZ}, \quad (46)$$

315 so that the enthalpy change equals the difference in Eq.(45). The heat capacities are evaluated as
 316 derivatives of the specific enthalpies of the phases:

$$\dot{m}_m^e \frac{\partial h_m}{\partial T} \Delta T + \dot{m}_s^e \frac{\partial h_s}{\partial T} \Delta T + \dot{m}_g^e \frac{\partial h_g}{\partial T} \Delta T = -\Delta \dot{H}_{RZ}. \quad (47)$$

The derivatives are estimated numerically

$$\dot{m}_m^e \frac{h_m(T'_2) - h_m(T'_1)}{T'_2 - T'_1} \Delta T + \dot{m}_s^e \frac{h_s(T'_2) - h_s(T'_1)}{T'_2 - T'_1} \Delta T + \dot{m}_g^e \frac{h_g(T'_2) - h_g(T'_1)}{T'_2 - T'_1} \Delta T = -\Delta \dot{H}_{RZ}, \quad (48)$$

where $T'_2 = T_{RZ}^e + 0.01$ and $T'_1 = T_{RZ}^e - 0.01$ are close to the current estimate for the reaction zone equilibrium temperature T_{RZ}^e . The masses are multiplied with the specific enthalpies and the enthalpies are summed

$$\frac{\dot{H}_m(T'_2) - \dot{H}_m(T'_1)}{T'_2 - T'_1} \Delta T + \frac{\dot{H}_s(T'_2) - \dot{H}_s(T'_1)}{T'_2 - T'_1} \Delta T + \frac{\dot{H}_g(T'_2) - \dot{H}_g(T'_1)}{T'_2 - T'_1} \Delta T = \frac{\dot{H}(T'_2) - \dot{H}(T'_1)}{T'_2 - T'_1} \Delta T = -\Delta \dot{H}_{RZ}, \quad (49)$$

where the temperature difference between the current equilibrium temperature and the new estimate can be solved:

$$\Delta T = \frac{-\Delta \dot{H}_{RZ}}{\frac{\dot{H}(T'_2) - \dot{H}(T'_1)}{T'_2 - T'_1}}. \quad (50)$$

The enthalpies in Eq. (49) are estimated using the Gibbs-Helmholz equation for the total Gibbs energy of the bulk phases. The Gibbs-Helmholz equations are estimated numerically using

$$H = \frac{\partial G/T}{\partial 1/T} = \frac{G(T'_2)/T'_2 - G(T'_1)/T'_1}{1/T'_2 - 1/T'_1}, \quad (51)$$

The new equilibrium temperature is calculated by adding the under-relaxed temperature difference to the last known value using similar kind of method as Eq. (16). The new temperature changes the equilibrium composition at the reaction zone and thus a new equilibrium has to be determined using PGE. The Gibbs energy minimization and the reaction zone temperature calculation are repeated successively and iteratively until the temperature difference predicted by Eq. (50) is smaller than a tolerance value.

4.2 Conservation of Energy and Mass

Mass and energy are conserved for the bulk liquid metal and slag phases in the converter model.

334 The conservation equation is discretized for the entire metal and slag bulk phases. A conservation
 335 equation for the enthalpy of the constituent mixture in phase is

$$\frac{\partial}{\partial t} \int h_{\text{mix}} \rho_{\text{mix}} dV = \frac{(h_{\text{mix}} \rho_{\text{mix}} V)^{n+1} - (h_{\text{mix}} \rho_{\text{mix}} V)^n}{\Delta t} = \dot{H}^e - \dot{H} - \varphi_h = \Psi, \quad (52)$$

336 where \dot{H}^e is the enthalpy flux coming from the reaction zone and \dot{H} is the enthalpy flux going into
 337 the reaction zone. Superscripts $n + 1$ and n indicate a new and old time level values, respectively.
 338 φ_h is a phase specific additional source term. In the case of slag φ_h is the heat source from lime
 339 dissolution. In the case of metal φ_h is the heat sink due to scrap melting. Subscript “mix” denotes
 340 component mixture. The mixture quantities are defined as

$$h_{\text{mix}} = \sum_i \frac{h_i \rho_i \alpha_i}{\rho_{\text{mix}}}, \quad \rho_{\text{mix}} = \sum_i \rho_i \alpha_i, \quad m_{\text{mix}} = \sum_i m_i, \quad (53)$$

341 where the sums are over all constituents in the bulk phase and α_i is the constituent volume fraction.
 342 The temperature of the phase is solved using the enthalpy method⁵¹. The mixture quantities are
 343 inserted into the new time level values and the equation is manipulated as follows:

$$\frac{(h_{\text{mix}} \rho_{\text{mix}} V)^{n+1} - (h_{\text{mix}} \rho_{\text{mix}} V)^n}{\Delta t} = \frac{(\sum_i h_i \rho_i \alpha_i V)^{n+1} - (h_{\text{mix}} m_{\text{mix}})^n}{\Delta t} = \frac{(\sum_i h_i m_i)^{n+1} - H_{\text{mix}}^n}{\Delta t}, \quad (54)$$

344 Next iteration index v is introduced and the enthalpy is linearized as

$$\begin{aligned} \frac{\partial h}{\partial T} &\approx \frac{h^{v+1} - h^v}{T^{v+1} - T^v}, \\ h^{n+1} &\approx h^{v+1} = h^v + \frac{\partial h}{\partial T} (T^{v+1} - T^v), \end{aligned} \quad (55)$$

345 which is substituted into Eq. (54):

$$\frac{(\sum_i h_i m_i)^{n+1} - H_{\text{mix}}^n}{\Delta t} = \frac{\sum_i m_i^v \left[h_i^v + \frac{\partial h_i^v}{\partial T} (T^{v+1} - T^v) \right] - H_{\text{mix}}^n}{\Delta t} = \frac{\sum_i m_i^v \left[\frac{\partial h_i^v}{\partial T} (T^{v+1} - T^v) \right] + H_{\text{mix}}^v - H_{\text{mix}}^n}{\Delta t} \quad (56)$$

346 After further manipulation the new temperature value can be solved:

$$\begin{aligned}
& \frac{\sum_i m_i^v \left[\frac{\partial h_i^v}{\partial T} (T^{v+1} - T^v) \right] + H_{\text{mix}}^v - H_{\text{mix}}^n}{\Delta t} = \Psi, \\
& \sum_i m_i^v \left[\frac{\partial h_i^v}{\partial T} (T^{v+1} - T^v) \right] = \Delta t \Psi - H_{\text{mix}}^v + H_{\text{mix}}^n, \\
& T^{v+1} = T^v + \frac{\Delta t \Psi - H_{\text{mix}}^v + H_{\text{mix}}^n}{\sum_i m_i^v \frac{\partial h_i^v}{\partial T}},
\end{aligned} \tag{57}$$

347 The enthalpy derivatives are multiplied with the masses and summed together

$$\sum_i m_i^v \frac{\partial h_i^v}{\partial T} = \sum_i \frac{\partial H_i^v}{\partial T} = \frac{\partial H_{\text{mix}}^v}{\partial T} = \frac{H_{\text{mix}}^v(T_2') - H_{\text{mix}}^v(T_1')}{T_2' - T_1'}, \tag{58}$$

348 where the Gibbs-Helmholtz equation is again used to estimate the solution enthalpies. The

349 conservation equation for phase constituent k mass is

$$\frac{\partial}{\partial t} \int \alpha_k \rho_k dV = \frac{(\alpha_k \rho_k V)^{n+1} - (\alpha_k \rho_k V)^n}{\Delta t} = \frac{m_k^{n+1} - m_k^n}{\Delta t} = \dot{m}_{k,\text{RZ}}^e - \dot{m}_{k,\text{RZ}} - \dot{\phi}_k, \tag{59}$$

350 where $\dot{m}_{k,\text{RZ}}^e$ is the mass flux of the component k coming from reaction zone, $\dot{m}_{k,\text{RZ}}$ is the mass flux

351 of the component leaving the from the phase and $\dot{\phi}_k$ is a phase specific additional source term. $\dot{\phi}_k$

352 is used for slag when adding lime during the process. $\dot{\phi}_k$ is used for metal melt when scrap is

353 melting and components are added to the phase.

354 4.3 Scrap Melting

355 Scrap is added to the process to keep the temperature from rising too high. The importance of scrap

356 melting on the dynamics of the BOF process is highlighted by the fact that the scrap weight is

357 typically 10-30 wt-% of the hot metal weight. Thus scrap melting is very important to take into

358 account. Since the scrap is usually low carbon steel, the carbon in the hot metal plays an important

359 role in the melting process. Namely carbon transports from the liquid to the surface of the scrap and

360 lowers the local melting point at the surface. Previously a scrap melting model with moving grid⁴¹

361 has been done. In this work a simplified version of this model is implemented. Instead of having a

362 1-d grid there is now a single balance area for the scrap enthalpy. Enthalpy balance equation for

363 scrap is given by

$$\frac{(hm)^{n+1} - (hm)^n}{\Delta t} = h_T A (T_{\text{metal}} - T_{\text{Liq}}) - \max(0, -\dot{m}_{\text{phase}}) H + \max(0, \dot{m}_{\text{phase}}) H_{\text{Liq}} = \Psi, \quad (60)$$

$$T^{v+1} = T^v + \frac{\Delta t \Psi - H^v + H^n}{m^v \frac{\partial h^v}{\partial T}},$$

where enthalpy method has been applied to solve the temperature. Details about this method in relation to scrap melting is in previous work⁴¹. Eq. (60) is combined with balance equations for enthalpy and carbon mass

$$U_{\text{IF}} \rho (H_{\text{liq}} - H_{\text{scrap}}) = k \frac{\partial T}{\partial x} - h_T (T_{\text{metal}} - T_{\text{liq}}) \quad (61)$$

$$U_{\text{IF}} (Y_{\text{liq}} - Y_{\text{scrap}}) = D_Y \frac{\partial Y}{\partial x} - h_Y (Y_{\text{metal}} - Y_{\text{liq}}) \approx -h_Y (Y_{\text{metal}} - Y_{\text{liq}})$$

at the solidus-liquidus interface which is located at the scrap surface. The carbon mass transfer from the liquid phase is assumed to advance as a moving solidus-liquidus interface. Therefore, the diffusion coefficient D_Y is assumed to be zero. From interface equations (61) the interface velocity U_{IF} and liquidus temperature Y_{liq} are solved. Using U_{IF} the mass that is melting or solidifying is calculated as:

$$\dot{m}_{\text{phase}} = U_{\text{IF}} \rho A, \quad (62)$$

and the total scrap mass is updated with

$$m^{n+1} = m^n + \Delta t \dot{m}_{\text{phase}}. \quad (63)$$

373

374

375

376

377

378

4.4 Thermodynamic Data and the Collection of Possible Stable Phases

The chemical reaction model contains three main bulk phases, which are liquid metal, slag and gas.

The metal phase contains also the solid scrap phase, which is exchanging heat and mass with it. The

metal phase constituents are Fe, C, Si and O. The bulk slag phase contains a liquid solution (CaO(l), SiO₂(l), FeO(l)) and possibly a number of solid phases (CaO(s), SiO₂(s), CaSiO₃(s), Ca₂SiO₄(s), Ca₃SiO₅(s), Ca₃Si₂O₇(s)). The gas phase consists of following constituents: O₂(g), CO(g) and CO₂(g). The reaction zone can contain all of the phases except the solid scrap.

386

The Gibbs free energies in standard state for compounds are calculated from heat capacity functions that are presented in Table 2. The first four columns give the coefficients for the polynomial functions that are from a publication of Taylor and Dinsdale⁵². The fifth and sixth columns give the temperature ranges for the polynomial at that particular row. The seventh and eighth columns give for the first row the enthalpy and entropy of a reference state, respectively and for the sequential rows the enthalpy and entropy of a phase transition. The rest of the polynomials are from HSC software⁵³. The enthalpy, entropy and Gibbs free energy are computed from the polynomials as follows:

$$\begin{aligned} H(T) &= H_{\text{ref}} + \int_{T_0}^{T_1} C_p dT + H_{\text{tr},1} + \dots + H_{\text{tr},n} + \int_{T_n}^T C_p dT, \\ S(T) &= S_{\text{ref}} + \int_{T_0}^{T_1} \frac{C_p}{T} dT + S_{\text{tr},1} + \dots + S_{\text{tr},n} + \int_{T_n}^T \frac{C_p}{T} dT, \\ G(T) &= H - TS, \end{aligned} \tag{64}$$

395

396

4.5 The Complete Algorithm

The solution of the mass and energy balances are advanced in time with the implicit Euler method. Thermodynamic equilibrium is calculated for the bulk slag phase and for the reaction zone. Flowcharts for time integration and for Gibbs energy minimization algorithms are presented in Fig. 1. In the beginning of time integration algorithm all necessary variables are initialized. Then according to the initial slag temperature and initial component masses thermodynamic equilibrium is calculated for bulk slag phase. Next for the initial time level the Gibbs energy is minimized as well as temperature of the reaction zone are iterated in a loop until the absolute temperature change

405 between iterations is less than 0.01 K. After initializations a loop begins for time integration. Inside
406 the time loop there is an iteration loop for implicit solution of the conservation equations. The
407 iteration loop continues until the absolute changes of the temperatures of the phases are less than
408 0.01 K. At the beginning of the iteration loop the mass constraints b_{RZ} of the reaction zone are
409 updated. The mass fluxes coming into the reaction zone are calculated using Eq. (41). The masses
410 are transformed into molar amounts and divided into specific components of the reaction zone.

411

412 Next the Gibbs energies for the reaction zone and slag phase are minimized and the thermodynamic
413 variables are updated, respectively. For the reaction zone the temperature is updated according to
414 Eq. (50) and for the slag phase from conservation Eq. (57). The slag mass constraints are solved
415 from the mass conservation Eq. (59). Then the melting rate of the scrap is determined and the scrap
416 temperature, mass and melting mass rate are solved. Finally the thermodynamic quantities of the
417 metal phase are updated as well as the conservation equations for energy and mass are solved,
418 respectively. The iteration loop ends with the update of the new time level values. The time
419 integration loop ends when maximum time value has been reached.

420

421 The “Gibbs energy minimization” algorithm has a loop containing equilibrium calculation using
422 PGE and a subroutine for checking the stabilities of phases. If the algorithm is started for the first
423 time, the initial condition is calculated using the Leveling and Post leveling methods. The estimate
424 after Post leveling is improved in PGE by assuming that the solution phases are ideal. After
425 initialization the non-ideal PGE is used with the activity models for liquid steel and slag phases.
426 When the “Gibbs energy minimization” routine is called during time integration, the initial
427 condition for PGE is the result from the previous iteration or time step. The loop is exited after the
428 “Check phase stabilities” routine is not changing the list of active (i.e. stable) phases.

429

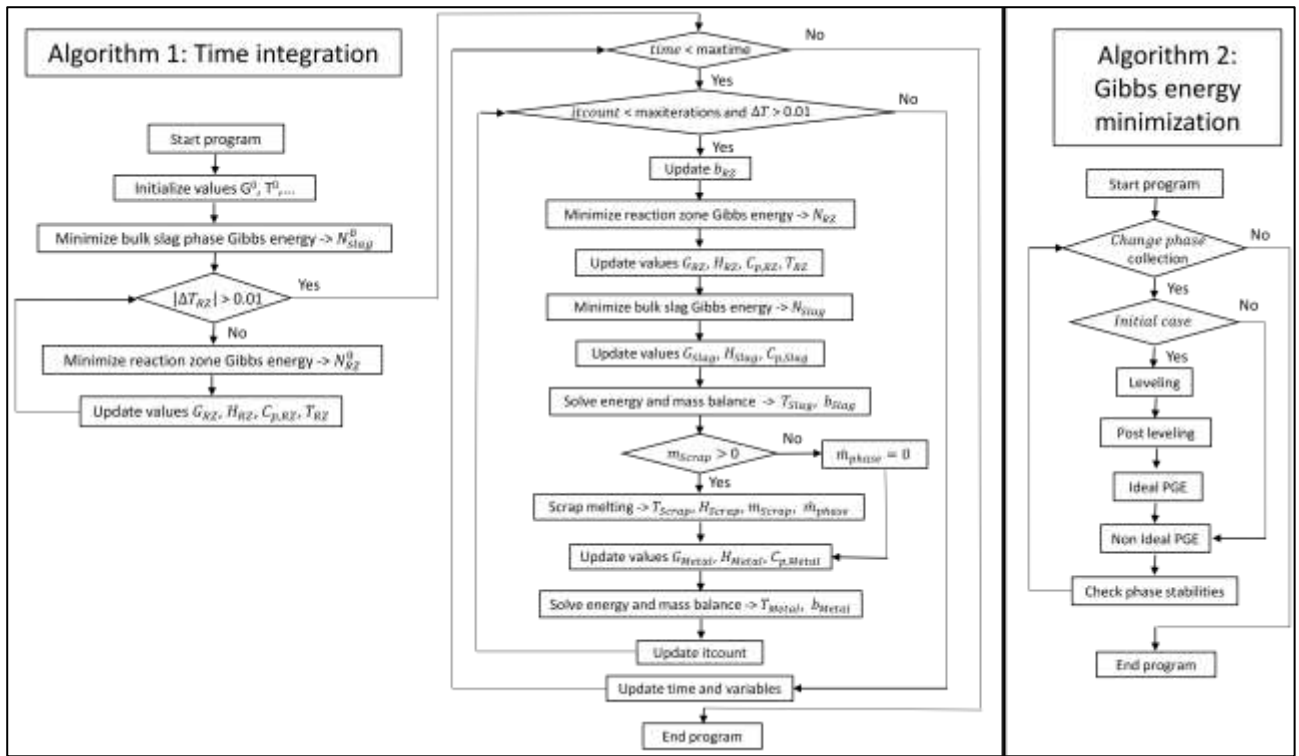


Fig. 1. Algorithms for time integration and for minimizing Gibbs energy

5 Validation and results

First the quasichemical model and pair fraction solution is validated by calculating iso-activity lines for liquid slag components SiO_2 and FeO . Finally the steel converter model is validated by comparing the metal and slag constituent concentrations to measurements of industrial scale converter.

5.1 Validation of the thermodynamic models

In Fig. 2 the calculated iso-activity lines in temperature 1550°C (1823 K) are compared with measurements⁵⁴. The agreement between the results is good.

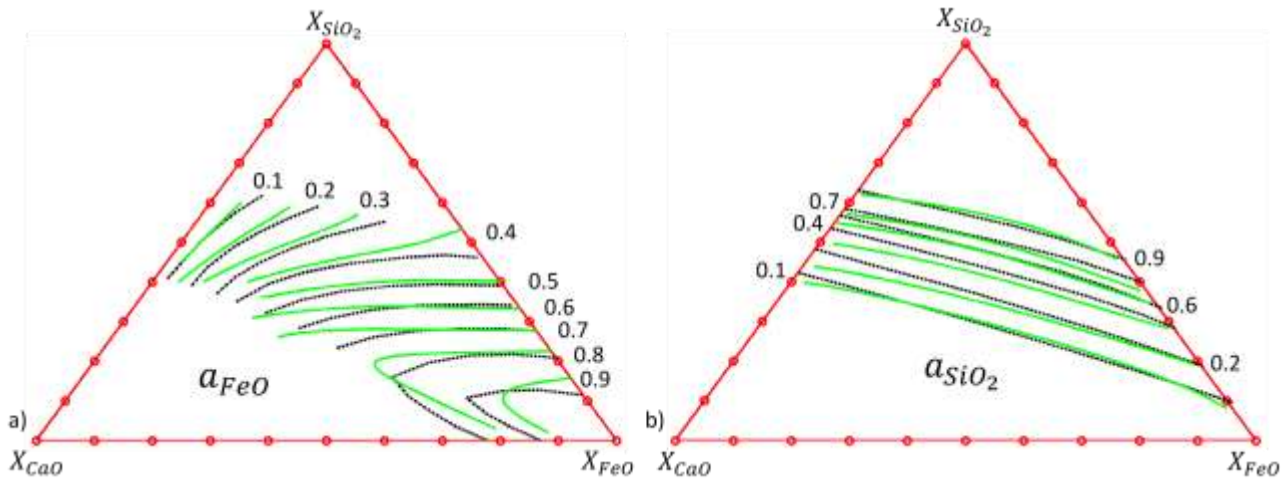
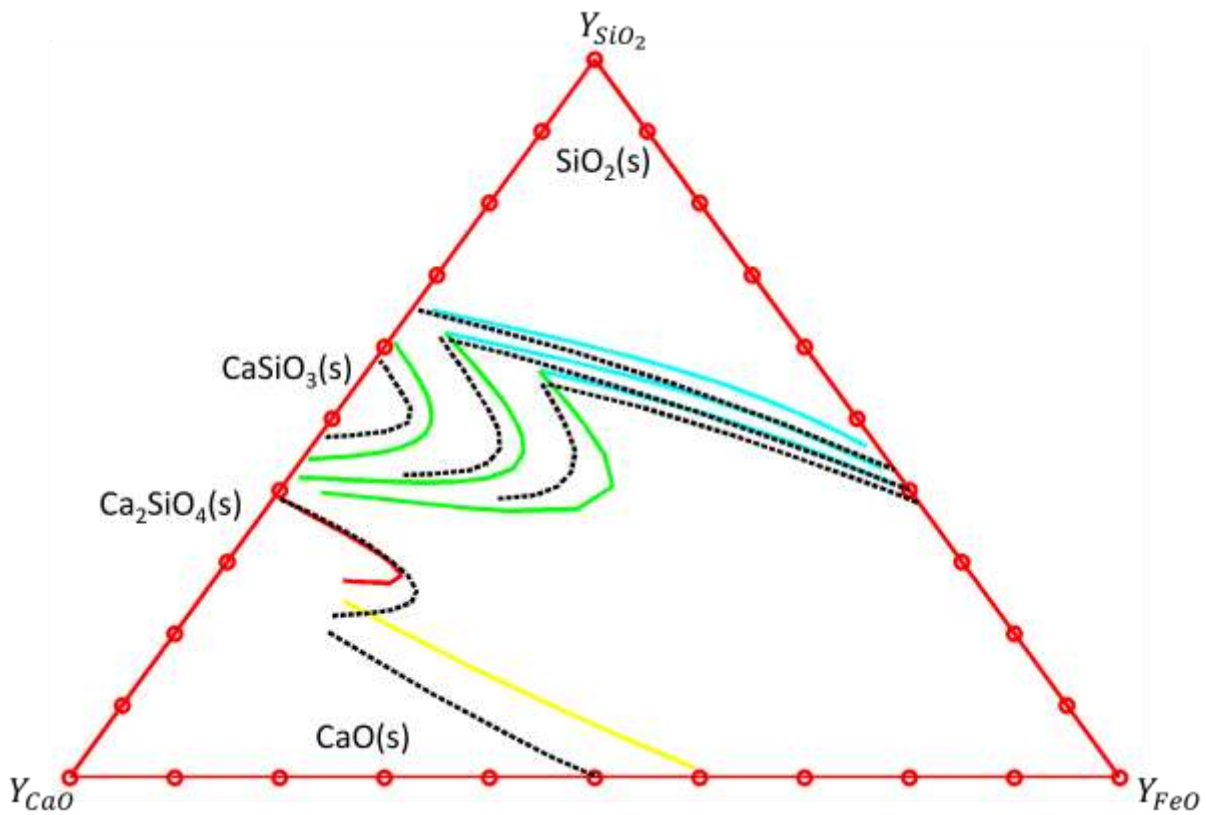


Fig. 2. Calculated iso-activity lines (solid green) compared with measurements (dashed black). a) FeO activities, b) SiO_2 activities

Next the PGE-algorithm with the quasichemical activity model is validated by calculating liquidus lines for $\text{SiO}_2(\text{s})$, $\text{CaSiO}_3(\text{s})$, $\text{CaO}(\text{s})$ and $\text{Ca}_2\text{SiO}_4(\text{s})$ compounds. The list of possible phases in the PGE include the liquid slag solution ($\text{CaO}(\text{l})$, $\text{SiO}_2(\text{l})$, $\text{FeO}(\text{l})$) and a number of solid phases ($\text{CaO}(\text{s})$, $\text{SiO}_2(\text{s})$, $\text{CaSiO}_3(\text{s})$, $\text{Ca}_2\text{SiO}_4(\text{s})$, $\text{Ca}_3\text{SiO}_5(\text{s})$, $\text{Ca}_3\text{Si}_2\text{O}_7(\text{s})$). A composition curve is setup inside the expected liquidus line and the PGE is started using the composition of the points of the curve as mass constraints. Then the PGE-algorithm determines the stable phases and the composition of the liquid phase, which forms the liquidus line. In Fig. 3 the calculated liquidus lines

453 for phases $\text{SiO}_2(\text{s})$ and $\text{CaSiO}_3(\text{s})$ at three temperatures, 1300°C (1573 K), 1400°C (1673 K) and
 454 1500°C (1773 K), are compared to measurements⁵⁵. Also computed liquidus lines for $\text{CaO}(\text{s})$
 455 and $\text{Ca}_2\text{SiO}_4(\text{s})$ in temperature 1900°C (2173 K) are compared with assumed liquidus lines⁵⁵. This
 456 is an estimate for maximal range in CaO rich side of the ternary for liquid slag in steel converter
 457 conditions. The accuracy for $\text{SiO}_2(\text{s})$ liquidus lines is more accurate than for the $\text{CaSiO}_3(\text{s})$
 458 compound. The worst accuracy appears to be for $\text{CaO}(\text{s})$ liquidus, although the exact liquidus in the
 459 ternary is not known. For the current objective in simulating the steel converter the accuracy is good
 460 enough. In future the phase diagram for the ternary will be improved.



461
 462 **Fig. 3. Calculated liquidus lines for CaSiO_3 (solid cyan) and SiO_2 (solid green) compounds at**
 463 **three temperatures ($T = 1300^\circ\text{C}$ (1573 K), 1400°C (1673 K), 1500°C (1773 K)) compared with**
 464 **measurements (dashed black). Calculated liquidus lines for $\text{CaO}(\text{s})$ (yellow) and $\text{Ca}_2\text{SiO}_4(\text{s})$**
 465 **(red) at temperature $T = 1900^\circ\text{C}$ (2173 K) compared with assumed liquidus lines (dashed**
 466 **black).**

467 5.2 Application to modelling of industrial practice

468 The converter model proposed in this work was validated using data published by Cicutti *et al.*⁵⁶.
469 They took several metal and slag samples from a 200 ton LD-LBE converter at different stages of
470 the process. The blow was interrupted for the duration of the sampling, and for this reason, only one
471 intermediate sample was taken per heat. At least five samples were taken per sampling point. The
472 size distribution and composition of the metal droplets extracted from the slag samples were also
473 analysed. The description of the blowing practice, additions and technical parameters of the vessel
474 are not repeated here.

475 5.2.1 Modelling parameters

476 One of the main adjustable parameters of the model are the mass flows of the metal, gas and slag
477 species. Only few correlations are available for mass transfer between hot metal and slag under
478 conditions comparable to those in the BOF process. The mass transfer models of Riboud and
479 Olette⁵⁷, Paul and Ghosh⁵⁸, and Hirasawa *et al.*⁵⁹ suggest that the proportionality of the mass
480 transfer coefficient to gas injection rate is to $\beta \propto \dot{V}_g^{1/2}$. In the BOF model of Kitamura *et al.*¹⁸, the
481 mass transfer coefficient in the slag phase was expressed as a function of bath volume, slag volume,
482 argon flow rate, CO generation rate, and solid fraction of the slag.

483

484 To simplify the description of the model, the mass flow of metal phase into the reaction zone was
485 assessed based on the results of Chatterjee *et al.*⁶⁰ from a 6 ton experimental BOF vessel. The
486 temperature of the metal bath was measured continuously and it was reported that under normal
487 blowing conditions, the temperature gradients in the metal bath varied from 10 to 40°C (10 to 40 K)
488 during the first part of the blow, although it was suggested that much higher temperature gradients
489 of 50 to 200°C (50 to 200 K) can exist under soft blowing conditions.

490

491 In addition to temperature measurements, Chatterjee *et al.*⁶⁰ took metal samples during processing
492 from two different bath depths. The carbon content in the upper part of the vessel was found to be

much lower than in the metal bath. The highest difference was measured between 25 and 50% of the blow. As suggested by Sarkar *et al.*²⁶, the difference in carbon content was approximately 0.17 to 0.18 wt-% during the main blow and 0.06 to 0.07 wt-% towards the end of the blow. By employing these values as the basis of their calculations, Sarkar *et al.*²⁶ estimated that the mass exchange rate between the lower and upper parts of the vessel should be in the order of 2500 kg/s under the conditions of the experiments reported by Cicutti *et al.*⁵⁶.

The bulk slag and metal initial temperature is 1347°C (1620 K). The initial carbon content in the bulk metal was taken as 4.5 wt-%, although Cicutti *et al.*⁵⁶ had an initial carbon concentration of 4.0 wt-%. The 0.5 w-% increase is to compensate for the omission of the Mn and P components. The slag components MnO, P₂O₅ and MgO are also omitted from the model. Thus the liquid slag can only contain FeO, CaO and SiO₂ components.

The top lance blow was continued for 16.5 minutes. The mass transfer parameter for bulk metal has a very small value in the first 20 seconds. After 20 seconds the parameter is increased incrementally to the steady-state value since it takes some time for the bulk metal phase to increase momentum due to the buoyancy forces. This modification leads to the oxidization of the iron in the reaction zone and very high temperatures during the first 20-30 seconds.

The mass transfer from metal phase due to bottom gas stirring is taken into account with

$$R_p = 1.79\sqrt{gH} \frac{\rho_m A_{\text{nozzle}}}{\rho_g \dot{V}_g}, \quad (65)$$

where g is gravitational accereleration, A_{nozzle} is the nozzle area and H is the plume height⁶¹. Eq. (65) is the ratio of liquid momentum at the surface level and gas momentum at the nozzle. The liquid mass transfer can be deduced from Eq. (65) and from plume momentum

$$I_m = \rho_m A v_m^2 = \dot{m}_m v_m, \quad (66)$$

where A is the plume area, v_m is the plume velocity and \dot{m}_m is the plume mass flux. A coefficient

517 of 0.554 was used instead of 1.79 in Eq. (65). The numerical results of Kärnä *et al.*⁶² suggest a linear
 518 relationship between the heat transfer coefficient and the lance height. In this work, it was assumed
 519 the relationship of the lance height and the mass transfer from the slag phase due to top-blowing is
 520 also linear. More specifically, the mass transfer is proportional to the oxygen mass flow rate \dot{m}_{O_2}
 521 and linearly dependent on the lance height d from the melt:

$$\begin{aligned} P_s &= \frac{\dot{m}_{O_2}}{m_{s,initial}} (C + Dd), \\ \dot{m}_s &= m_s P_s, \end{aligned} \quad (67)$$

522 The coefficient $C = 1.13$ as well as $D = -0.29 \text{ 1/m}$ were fitted using the data of Cicutti *et al.*⁵⁶.
 523 Due to the high initial temperatures radiation transport is added to the reaction zone temperature
 524 iteration. Eq. (50) is modified into

$$\begin{aligned} \Delta T &= \frac{-h_{\text{rad}}(T^v - T_{\text{ext}}) - \Delta \dot{H}_{\text{RZ}}}{C_{p,\text{RZ}} + h_{\text{rad}}}, \\ h_{\text{rad}} &= A_{\text{rad}} \sigma \xi (T^{v,3} + T^{v,2} T_{\text{ext}} + T^v T_{\text{ext}}^2 + T_{\text{ext}}^3), \end{aligned} \quad (68)$$

525 where A is the radiation transport area, $\sigma = 5.67 \times 10^{-8} \text{ W/m}^2\text{K}^4$ is the Stefan-Boltzmann
 526 constant, ξ is the surface emissivity and T_{ext} is the external temperature. Eq. (68) estimates the
 527 radiation exchange between the reaction zone and the converter interior. Here, implicit
 528 discretization has been applied to the radiation term. The heat radiation has a cooling effect on the
 529 temperature of the reaction zone.

530

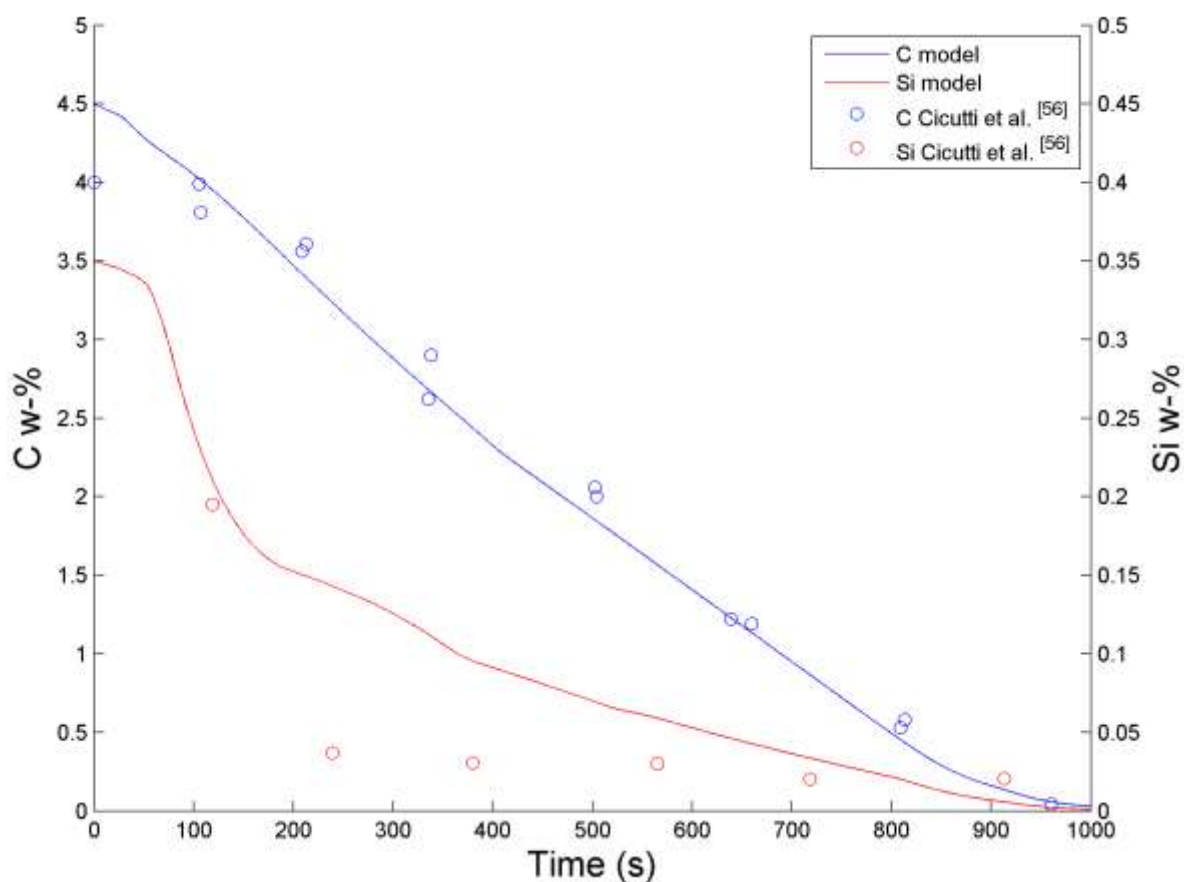
531 Table 3 shows the main process parameters employed in the simulations. More details can be found
 532 from the work Cicutti *et al.*⁵⁶. The results were calculated using 1s time-step. The calculations were
 533 repeated using a 0.25 s time-step and the results were identical.

534

535 5.2.2 Modelling results

536 Fig. 5 shows the predicted carbon and silicon content in comparison to the experimental data of
 537 Cicutti *et al.*⁵⁶. The Si component concentrations have a second y-axis in the figure. The Si

538 component is oxidised first as is suggested by the measurements. The Si concentration is somewhat
 539 high compared to measurements during 200 and 700s, which can be attributed in part to the fact that
 540 P and Mn are ignored in the system. Also the missing slag components MnO and MgO are known
 541 to decrease the activity of SiO_2 ⁶³ and thus can cause the difference in the results. The Si
 542 concentration is lower at the end of the blow, which can be due to high oxygen content of the bulk
 543 metal. The carbon concentration agrees very well with the measurements.



544
 545 **Fig. 4. Carbon and silicon concentrations in bulk metal as a function of time.**

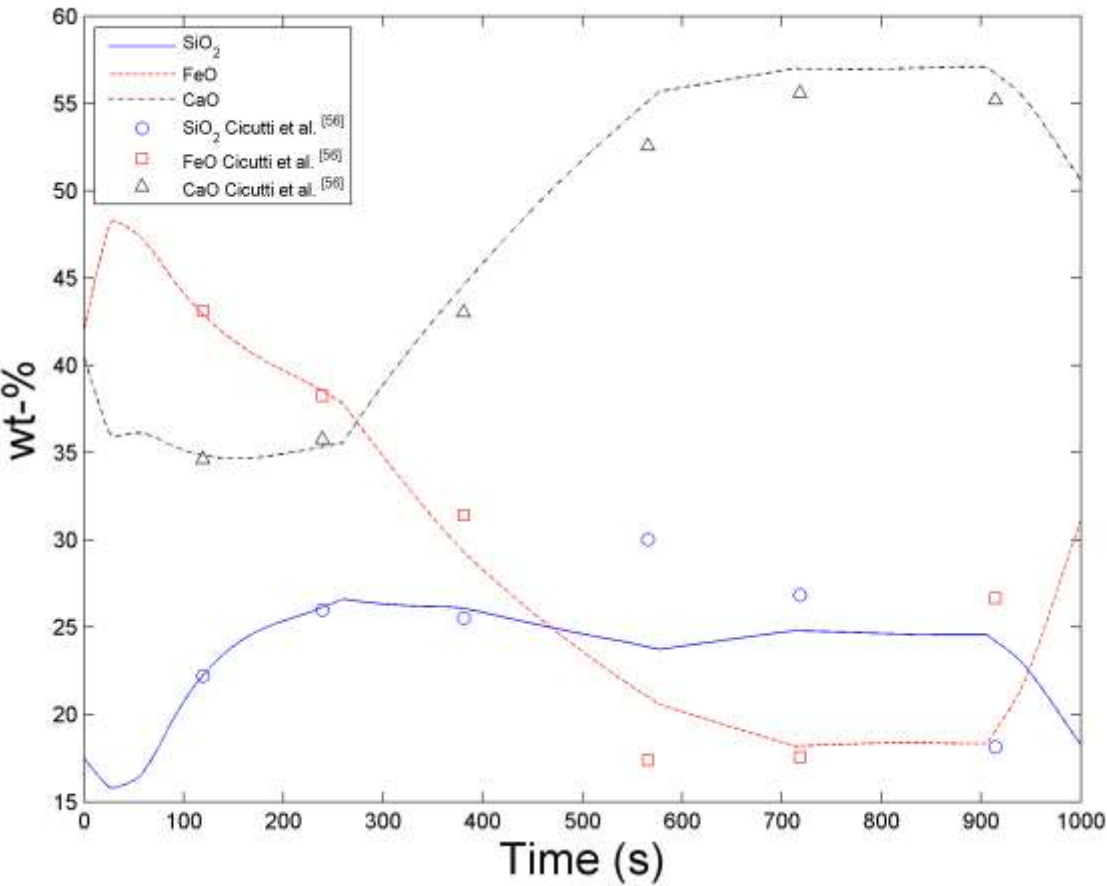
546
 547 The liquid slag composition as a function of time is presented in Fig. 5. The measurements of
 548 Cicutti for CaO, FeO and SiO_2 have been normed to 100% to make the comparison with the model
 549 more appropriate. At the initial stage iron is oxidized due to poor mixing in the metal phase.
 550 Afterwards FeO oxidizes components from the metal and is decreasing in the liquid slag phase. The
 551 SiO_2 concentration is noticeably increasing from 50 s to 250 s, when most of the Si is oxidized from

the metal phase. CaO concentration starts to increase after 240 s, when constant 8 kg/s dissolution rate is set to start in the model. The total lime (CaO) amount added during the process is approx. 6000 kg. The dissolved CaO is available in the thermodynamic equilibrium calculation for the bulk slag phase. Around 900 s iron starts to oxidize due to the low carbon concentration in the bulk metal. Overall the results match with the measurements very well.

The temperature evolution of the bulk metal and the reaction zone are presented in Fig. 6. In the beginning the metal mass transfer to the reaction zone is very poor. This leads to high overall oxidization of the components in the metal phase at the reaction zone resulting in very high temperatures. After 20 s, the temperature of the reaction zone decreased rapidly, when the momentum starts to build up in the metal phase. This is taken into account by increasing the mass transfer coefficient incrementally. The metal phase temperature is decreasing due to the scrap melting. After 100 s the temperatures start to increase up until to the end of the blow. At the 900 s point the reaction zone temperature rise stalls due to the increased argon bottom stirring.

In many of the earlier-proposed mathematical models for the BOF process,^{19,20,21,22,23,24,25,26} the fraction of solid compounds in the slag during the blow has been extracted from the kinetics of lime dissolution without explicitly calculating the saturation of CaO. One of the advantages of the model proposed in this work is that it calculated the precipitation of solid compounds based on Gibbs free energy minimization. Fig. 7 shows the predicted solid mole fraction in the slag a) and the molar % of solid component in the total moles of solids b). At the 580 s point solid components start to be stable with the liquid slag. This happens because the FeO content is decreasing and the CaO is dissolving continuously. The solid material in equilibrium increase until about 250 s and afterwards decrease due to rising temperatures and rising FeO content in the slag. Two solid components CaO(s) and Ca₃SiO₅(s) are stable during the solidification as can be seen from Fig. 7 b). In the beginning of solidification all of the solid is CaO(s). Between 715 s and 905 s also Ca₃SiO₅(s) is a

578 stable phase.



579

580 **Fig. 5. Bulk slag composition as a function of time.**

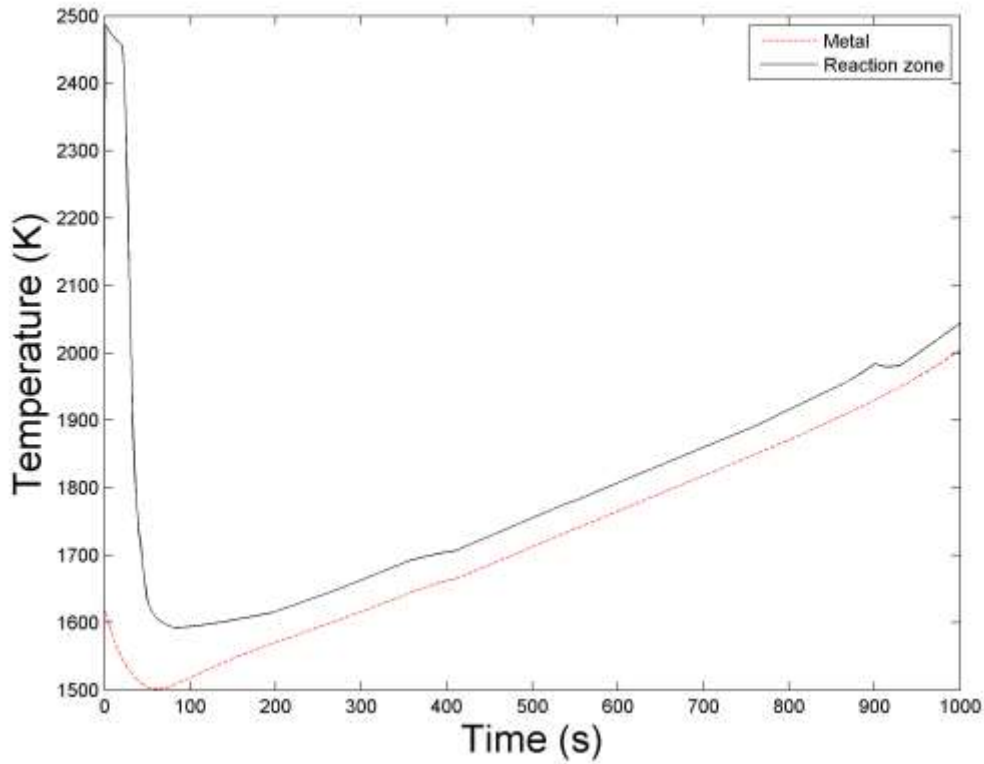


Fig. 6. The bulk metal and reaction zone temperatures as a function of time.

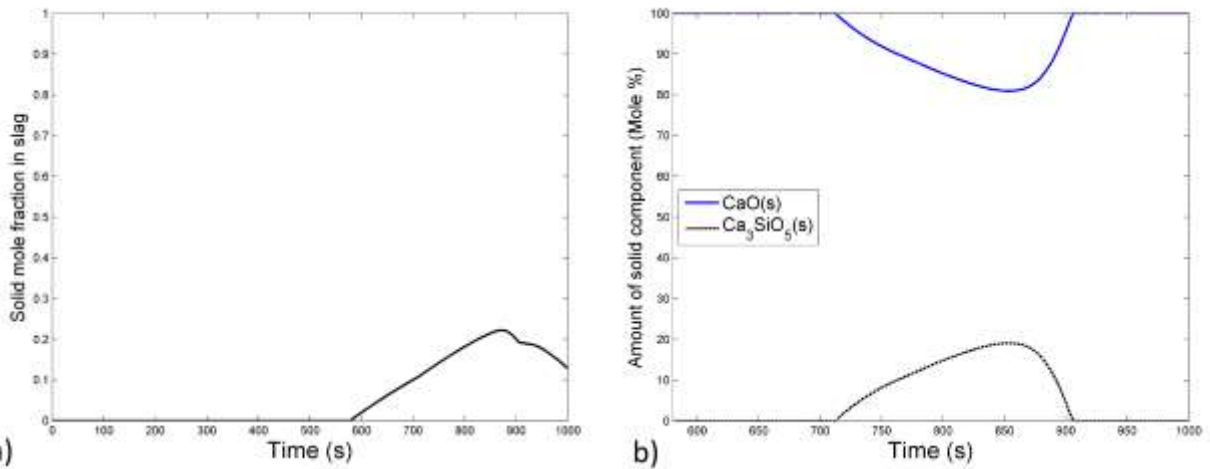


Fig. 7. Bulk slag solid mole fraction as a function of time a) and the amount of two solid components b).

It should be noted that the data of Cicutti *et al.*⁵⁶ has been employed by Dogan *et al.*²⁰ and Sarkar *et al.*²⁶ for the validation of their mathematical models, and therefore, a direct comparison with the results obtained with their models is permissible. A comparison between the slag composition and the work of Sarkar *et al.*²⁶ is presented in Fig. 8a to Fig. 8c. The data of Sarkar have been scaled so

that the sum of the three components is equal to 100%. Here, considerable improvements have been made in the accuracy especially for CaO and FeO concentrations. The carbon concentration in the iron melt is compared with Sarkar et al. and with Dogan et al.²⁰ in Fig. 8d. Although the accuracy of the models is similar during the middle stage of the process, the model proposed in this work provides a better description of the latter part of the process.

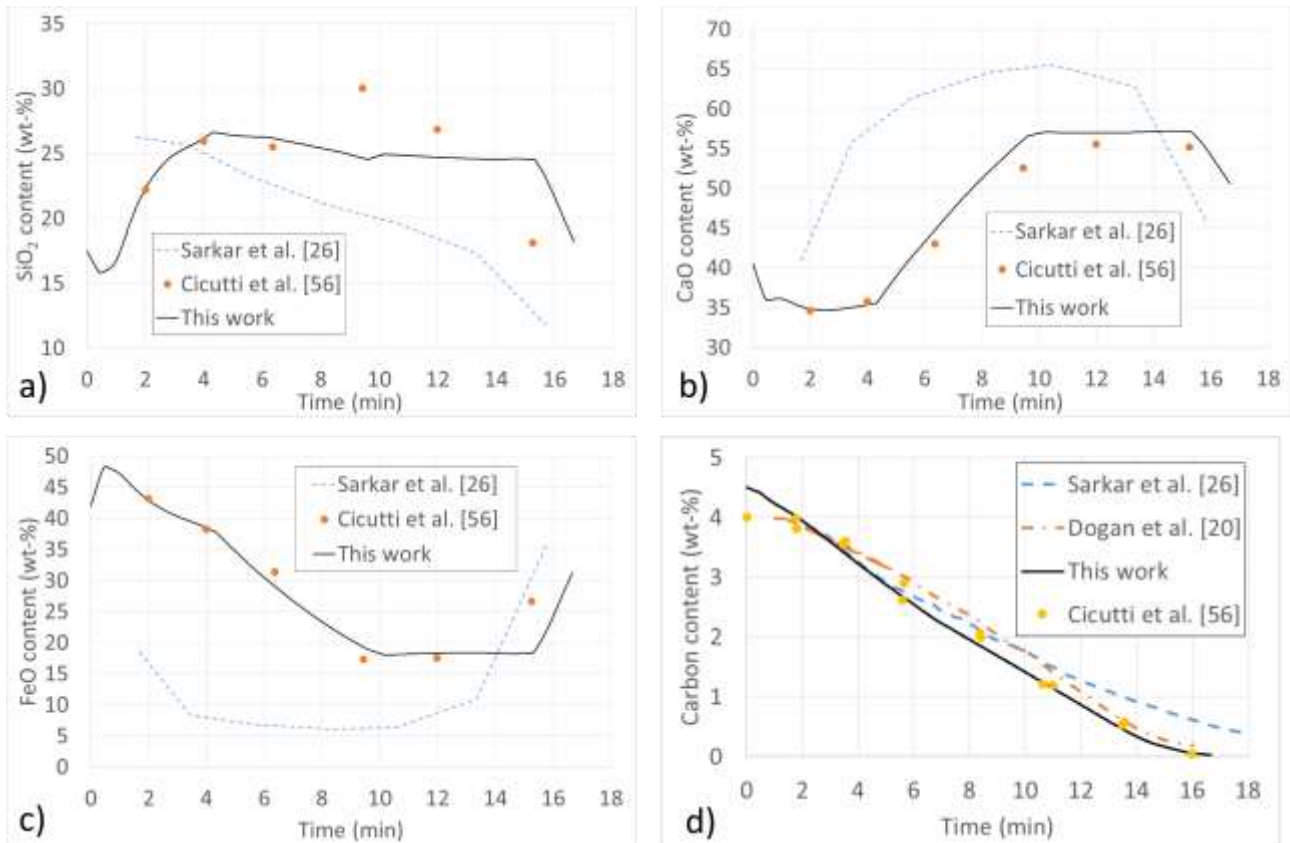
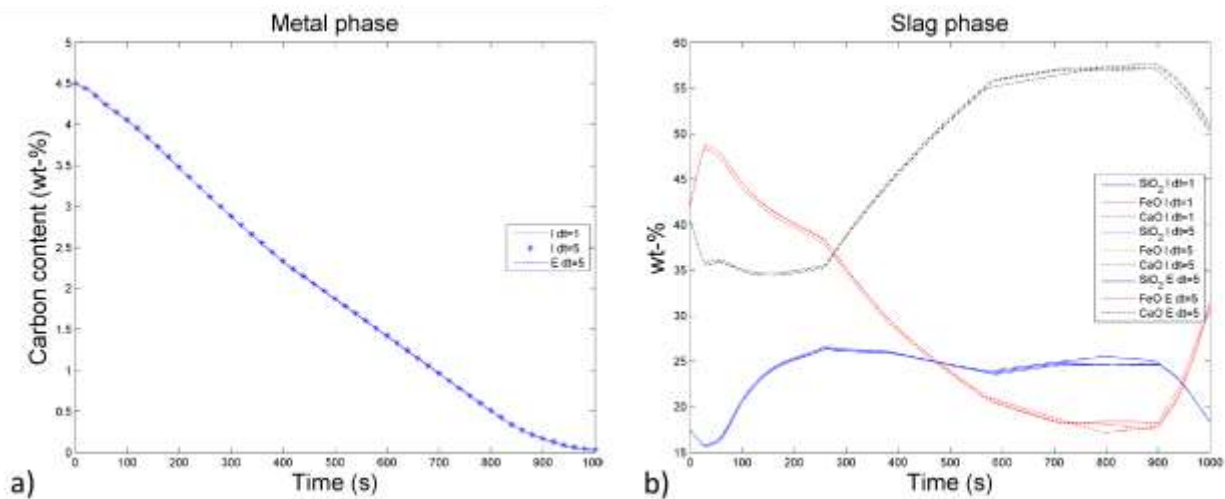


Fig. 8. Comparison of the slag composition (a,b,c) and comparison of the carbon content in iron in fig. d with literature.

Table 4 shows a comparison of the predicted carbon contents with experimental data, as well as with the results of Sarkar *et al.*²⁶ and Dogan *et al.*²⁰. It can be seen that the error in the predicted carbon content was lower than that obtained with the models proposed by Sarkar *et al.*²⁶ and Dogan *et al.*²⁰ both in terms of the mean absolute error (MAE) and the root-mean-square error (RMSE).

One of the objectives of the proposed chemical reaction model was the ability for real-time calculation of a steel converting process. Therefore, the Matlab program was tested for computation

607 time using two different time steps $dt = 1\text{ s}$ and $dt = 5\text{ s}$. The total calculation times for these
608 time steps were 48 min ($dt = 1\text{ s}$) and 15 min 35 s ($dt = 5\text{ s}$). This indicates that real time
609 computation of the process is possible with the current Matlab implementation using the longer time
610 step. As was mentioned earlier, the implicit Euler method was employed for time integration. To
611 achieve an even faster computational speed, an explicit Euler time integration was also tested with
612 $dt = 5\text{ s}$. The total computing time was 12 min, which suggests that the model is sufficiently fast
613 for online use. In Fig. 9 a comparison of these three different cases is presented. It can be seen that
614 there is virtually no difference in the composition evolution in metal and slag phases. Also, it should
615 be noted that since the model was executed in Matlab – a script language – the computing time
616 could be reduced considerably by executing the model in a compiled language such as C++. A four
617 core CPU was used to calculate the cases in this work. During the Matlab calculations according to
618 Windows Task Manager the CPU usage was in the range of 12-15% of total computing resources.
619 Therefore, if the cores of the processor can be utilized in full many reaction zones can be added into
620 the model without increasing the computing time.



621
622 **Fig. 9. Comparison of the implicit and explicit Euler algorithm with $dt = 1\text{ s}$ and $dt = 5\text{ s}$.**
623 **a) Comparison for carbon concentration in metal phase. b) Comparison for component**
624 **concentrations in slag phase.**

625 **6 Conclusions**

626 In earlier work, mathematical models were derived for scrap melting and bottom blowing in the
627 BOF process to provide a basis for a comprehensive BOF process model. In continuation of this
628 work, the present paper represents a first step towards mathematical modelling of reactions during
629 the top-blowing in BOF steelmaking. An implementation of the full chemical reaction model has
630 been developed in Matlab in this work. At this point, the model focuses on the oxidation of carbon
631 and silicon in the metal bath. The Partitioning of Gibbs energy method, in combination with
632 suitable descriptions for the excess Gibbs free energy, was found to provide robust solution of
633 complex metal-slag-gas equilibria under conditions of top blowing decarburisation. In the liquid
634 slag phase modified quasichemical model was applied to take into account the excess Gibbs energy
635 for the components. A method for the pair fraction calculation in MQM was introduced in the
636 paper. This method is readily expandable to increase the number of slag components.

637

638 The results from validation of the model with experimental data suggest that the model is able to
639 capture the main trends in the evolution of the metal and slag compositions with a reasonably good
640 degree of accuracy. Based on comparison of the results with those by Sarkar et al.²⁶ and Dogan et
641 al.²⁰, it was found that the model proposed in this work provides a higher degree of accuracy in
642 relation to composition trends. Making use of the reaction volume approach, the model can be
643 extended to include new reaction zones and reactions, such as the oxidation reactions of manganese
644 and phosphorous. The principles presented in this paper are readily applicable in many other high
645 temperature processes. The real time requirement of the proposed model was confirmed in test
646 calculations.

647

648 In future possible additional reaction zone could be between the argon gas bubbles and the metal
649 plume. In the second reaction zone solute oxygen from metal can transfer into the gas bubbles and
650 leave the metal phase. Also additional oxidation of carbon can be introduced in this way. A third

651 reaction zone could be between the slag and the post combustion of the rising CO gas from the first
652 reaction zone. The third reaction zone would produce more heat into the slag phase.
653

654 **7 Acknowledgements**

655 This work was partly funded by the Finnish Funding Agency for Technology and Innovation
656 (TEKES). The research was carried out within the framework of the DIMECC SIMP research
657 program.

658

659 Appendix 1. Initial values for pair fractions

660 Before starting the algorithm for the solution of the pair fractions a reasonably good initial guess
 661 should be generated. This can be done by inserting the Eq. (37) into Eq. (36). After reorganizing
 662 this produces three equations

$$\begin{aligned} X_{AB}^2(1 - K_{AB}) + X_{AB}(X_{AC} + X_{BC} - 2Y_A - 2Y_B) + 4Y_A Y_B - 2(X_{BC} Y_A + X_{AC} Y_B) + X_{AC} X_{BC} &= 0, \\ X_{AC}^2(1 - K_{AC}) + X_{AC}(X_{AB} + X_{BC} - 2Y_A - 2Y_C) + 4Y_A Y_C - 2(X_{BC} Y_A + X_{AB} Y_C) + X_{AB} X_{BC} &= 0, \\ X_{BC}^2(1 - K_{BC}) + X_{BC}(X_{AB} + X_{AC} - 2Y_B - 2Y_C) + 4Y_B Y_C - 2(X_{AC} Y_B + X_{AB} Y_C) + X_{AB} X_{AC} &= 0, \end{aligned} \quad (69)$$

663 where $K_{AB} = \exp\left(\frac{\Delta g_{AB}}{RT}\right)$, etc. These equations are only functions of (X_{AB}, X_{AC}, X_{BC}) . By subtracting
 664 the second row equation from the first row equation, subtracting the third row equation from the
 665 first row equation and subtracting the second row equation from the third row equation again three
 666 equations are obtained:

$$\begin{aligned} X_{AB}^2(1 - K_{AB}) + 2X_{AB}(2Y_C - 1) + 4Y_A Y_B - X_{AC}^2(1 - K_{AC}) - 2X_{AC}(2Y_B - 1) - 4Y_A Y_C &= 0, \\ X_{AB}^2(1 - K_{AB}) + 2X_{AB}(2Y_C - 1) + 4Y_A Y_B - X_{BC}^2(1 - K_{BC}) - 2X_{BC}(2Y_A - 1) - 4Y_B Y_C &= 0, \\ X_{BC}^2(1 - K_{BC}) + 2X_{BC}(2Y_A - 1) + 4Y_B Y_C - X_{AC}^2(1 - K_{AC}) - 2X_{AC}(2Y_B - 1) - 4Y_A Y_C &= 0, \end{aligned} \quad (70)$$

667 The advantage of this manipulation is that now each equation is only dependent on two unknown
 668 pair fractions. Also in Eqs. (70) there are no terms in these equations where two pair fractions are
 669 multiplying each other like in Eqs. (69). By applying the solution of second degree polynomial
 670 equation to the first row equation we get

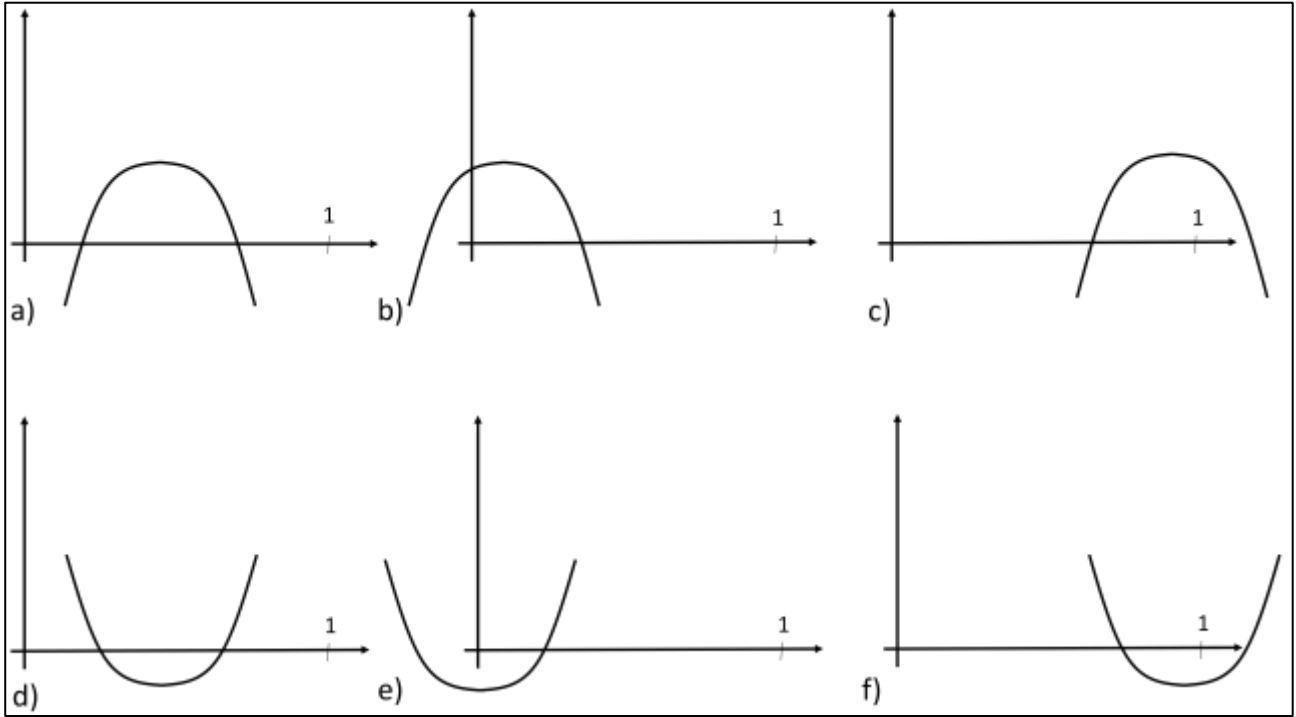
$$\begin{aligned} X_{AB} &= \frac{-B_{AB} \pm \sqrt{B_{AB}^2 - 4A_{AB}(C_{AB} - A_{AC}X_{AC}^2 - B_{AC}X_{AC} - C_{AC})}}{2A_{AB}} \\ A_{AB} &= (1 - K_{AB}), \quad A_{AC} = (1 - K_{AC}) \\ B_{AB} &= 2(2Y_C - 1), \quad B_{AC} = 2(2Y_B - 1) \\ C_{AB} &= 4Y_A Y_B, \quad C_{BC} = 4Y_A Y_C \end{aligned} \quad (71)$$

671 where the coefficients are the terms multiplying the pair fractions in Eq. (70). So that X_{AB} could
 672 have any real solutions the determinant should be either zero or positive:

$$4A_{AB}(A_{AC}X_{AC}^2 + B_{AC}X_{AC} + C_{AC} - C_{AB}) + B_{AB}^2 \geq 0, \quad (72)$$

673 Using Eq. (72) limits can be acquired for pair fraction X_{AC} . In Fig. 10 all possible parabolas are
 674 presented, which give limiting values for the pair fraction and have positive values for Eq. (72)

675 between $X = [0,1]$. If product $A_{AB}A_{AC}$ is negative, the parabola is opening down (Fig. 10a,b,c). If
 676 the product is positive, the parabola is opening up (Fig. 10d,e,f). For clarification, there are more
 677 possibilities for parabolas which give positive values when $X = [0,1]$, but these will not give new
 678 limits that are between $[0,1]$. It is now assumed that Eq. (72) has two solutions X_1 and X_2 as well as
 679 $X_1 < X_2$. If the parabola is opening down, the limiting values for X_{AC} must be between the two
 680 solutions.



681
 682 **Fig. 10. All possible parabolas from a) to f) for Eq. (72) that can give limiting values for pair**
 683 **fraction.**

684
 685 Since fractions can have values only between zero and one, the new limiting values for X_{AC} can be
 686 calculated as follows:

$$L_{AC} = \max(X_1, 0) \quad U_{AC} = \min(X_2, 1), \quad (73)$$

687 where L_{AC} is the lower limit and U_{AC} is the upper limit. The upward opening parabola can give two
 688 ranges for limits that are between $[0,1]$. This happens when $0 \leq X_1, X_2 \leq 1$. The corresponding
 689 situation is in Fig. 10d. Then the first limits are

$$L_{AC}^1 = 0 \quad U_{AC}^1 = X_1, \quad (74)$$

690 and the second limits are

$$L_{AC}^2 = X_2 \quad U_{AC}^2 = 1. \quad (75)$$

691 The correct solution has to be between the first lower and upper limits or the second lower and
 692 upper limits. Using the Eqs. (70) similarly as above limits can be acquired for the three pair
 693 fractions (X_{AB}, X_{AC}, X_{BC}). Additional improvements in the initial guesses can be achieved by
 694 inserting the limiting values for X_{AC} in Eq. (71) and studying whether the solutions for X_{AB} are even
 695 more limiting than the previous limits. This second step was noticed to usually decrease the limits
 696 from previous values. Finally the initial guesses are calculated as averages of the lower and upper
 697 limits:

$$X_{AC} = 0.5(L_{AC} + U_{AC}), \quad X_{AB} = 0.5(L_{AB} + U_{AB}), \quad X_{BC} = 0.5(L_{BC} + U_{BC}). \quad (76)$$

698 Initial values for the three other pair fractions can now be calculated from Eqs. (37).

699 **Nomenclature**

700	ρ	Density (kg/m^3)
701	A	Area (m^2)
702	V	Volume (m^3)
703	m	Mass (kg)
704	\dot{m}	Mass flux (kg/s)
705	t	Time (s)
706	G	Gibbs energy (J/)
707	R	Universal gas constant (J/(mol*K))
708	T	Temperature (K)
709	g	Dimensionless Gibbs energy and gravitational acceleration (m/s^2) in Chapter 0
710	x, X	Mole fraction
711	Y	Mass fraction
712	μ	Chemical potential of constituent (J/mol)
713	n	Molar amount (mol)
714	b	Mass constraint
715	a_{ij}	Stoichiometric matrix
716	F	Number of degrees of freedom
717	C	Number of components
718	Φ	Total number of phases
719	Γ	Dimensionless chemical potential of component
720	J	Jacobian matrix
721	D	Dimensionless driving force
722	γ	Activity coefficient
723	ε	First order interaction parameter

724	Δg	Gibbs energy of pair formation
725	Z	Coordination number
726	Y	Mass fraction and coordination equivalent fraction in Chapter 3.2
727	q	Gibbs energy coefficient of the pair fraction polynomial (J/mol)
728	ω	Temperature independent part of the Gibbs energy coefficient (J/mol)
729	η	Temperature dependent part of the Gibbs energy coefficient (J/(mol*K))
730	\dot{V}	Volume flow rate (m^3/s)
731	H	Enthalpy (J)
732	S	Entropy (J/(mol*K))
733	\dot{H}	Enthalpy flux (J/s)
734	h	Specific enthalpy (J/kg)
735	c_p	Heat capacity (J/(kg*K))
736	φ	Enthalpy or mass source (J/s), (kg/s)
737	α	Volume fraction
738	h_T	Heat transfer coefficient (W/(m ² *K))
739	h_Y	Mass transfer coefficient (m/s)
740	k	Thermal conductivity (W/(m*K))
741	I	Momentum (kg*m)/s ²
742	v	Velocity (m/s)
743	R_p	plume momentum ratio (dimensionless)
744		
745		
746	Subscripts	
747	g	gas
748	m	metal
749	s	slag
750	mix	mixture

751	i, j, l, k	generic indices
752	A, B, C	components A, B and C
753	RZ	reaction zone
754	Liq	liquidus
755	T	temperature
756	IF	interface
757	ref	reference
758		
759	Superscripts	
760	ex	excess Gibbs energy
761	°	standard state
762	p	pure phase
763	s	solution phase
764	v	iteration index
765	n	time level
766	e	equilibrium
767		
768		
769		

- ¹ N. Molloy: *J. Iron Steel Inst.*, 1970, vol. 208, pp. 943–950.
- ² F.-R. Block, A. Masui and G. Stolzenberg: *Arch. Eisenhüttenwes.*, 1973, vol. 44, pp. 357–361.
- ³ W. Kleppe and F. Oeters: *Arch. Eisenhüttenwes.*, 1976, vol. 47, pp. 271–275.
- ⁴ F. R. Cheslak, J. A. Nicholls and M. Sichel: *J. Fluid Mech.*, 1969, vol. 36, pp. 55–63.
- ⁵ Subagyo, G. A. Brooks, K. S. Coley and G. A. Irons: *ISIJ Int.*, 2003, vol. 43, pp. 983–989.
- ⁶ B. K. Rout, G. Brooks, Subagyo, M. A. Rhamdhani and Z. Li: *Metall. Mater. Trans. B*, 2016, vol. 47, pp. 3350–3361.
- ⁷ S. C. Koria and K. W. Lange: *Metall. Trans. B*, 1984, vol. 15, pp. 109–116.
- ⁸ S. C. Koria and K. W. Lange: *Ironmaking Steelmaking*, 1986, vol. 13, pp. 236–240.
- ⁹ R. C. Urquhart and W. G. Davenport: *Can. Metall. Q.*, 1973, vol. 12, pp. 507–516.
- ¹⁰ E. Schürmann, G. Mahn, J. Schoop and W. Resch: *Arch. Eisenhüttenwes.*, 1977, vol. 48, pp. 515–519.
- ¹¹ T. Kootz, K. Behrens, H. Maas and P. Baumgarten: *Stahl Eisen*, 1965, vol. 85, pp. 857–865.
- ¹² F. Oeters: *Arch. Eisenhüttenwes.*, 1966, vol. 37, pp. 209–219.
- ¹³ K. W. Lange: *Arch. Eisenhüttenwes.*, 1971, vol. 42, pp. 233–241.
- ¹⁴ K. Koch, W. Fix and P. Valentin: *Arch. Eisenhüttenwes.*, 1976, vol. 47, pp. 659–663.
- ¹⁵ K. Koch, W. Fix and P. Valentin: *Arch. Eisenhüttenwes.*, 1978, vol. 49, pp. 109–114.
- ¹⁶ S. Asai and I. Muchi: *Trans. Iron Steel Inst. Jpn*, 1970, vol. 10, pp. 250–263.
- ¹⁷ K.-C. Chou, U. B. Pal and R. G. Reddy: *ISIJ Int.*, 1993, vol. 33, pp. 862–868.
- ¹⁸ S.-Y. Kitamura, H. Shibata and N. Maruoka: *Steel Res. Int.*, 2008, vol. 79, pp. 586–590.
- ¹⁹ F. Pahlevani, S. Kitamura, H. Shibata and N. Maruoka: *Steel Res. Int.*, 2010, vol. 81, pp. 617–622.
- ²⁰ N. Dogan, G. A. Brooks and M. A. Rhamdhani: *ISIJ Int.*, 2011, vol. 51, pp. 1086–1092.
- ²¹ N. Dogan, G. A. Brooks and M. A. Rhamdhani: *ISIJ Int.*, 2011, vol. 51, pp. 1093–1101.
- ²² N. Dogan, G. A. Brooks and M. A. Rhamdhani: *ISIJ Int.*, 2011, vol. 51, pp. 1102–1109.
- ²³ A. K. Shukla, B. Deo, S. Millman, B. Snoeijer, A. Overbosch and A. Kapilashrami: *Steel Res. Int.*, 2010, vol. 81, pp. 940–948.
- ²⁴ Y. Lytvynnyuk, J. Schenk, M. Hiebler and A. Sormann: *Steel Res. Int.*, 2014, vol. 85, pp. 537–543.
- ²⁵ Y. Lytvynnyuk, J. Schenk, M. Hiebler and A. Sormann: *Steel Res. Int.*, 2014, vol. 85, pp. 544–563.
- ²⁶ S. Sarkar, P. Gupta, S. Basu and N. B. Ballal: *Metall. Mater. Trans. B*, 2015, vol. 46, pp. 961–976.
- ²⁷ M. Han, Y. Li and Z. Cao, *Neurocomputing*, 2014, vol. 123, 415–423.
- ²⁸ M. Han and C. Liu, *Appl. Soft Comput.*, 2014, vol. 19, pp. 430–437.
- ²⁹ H.-J. Odenthal, N. Uebber, J. Schlüter, M. Löpke, K. Morik and H. Blom: *Stahl Eisen*, 2014, vol. 134, pp. 62–67.
- ³⁰ D. Laha, Y. Ren and P. N. Suganthan: *Expert Syst. Appl.*, 2015, vol. 42, pp. 4687–4696.
- ³¹ A. Sorsa, J. Ruuska, J. Lilja and K. Leiviskä: *IFAC-PapersOnLine*, 2015, vol. 48, pp. 177–182.
- ³² K. Koch, W. Fix and P. Valentin: *Arch. Eisenhüttenwes.*, 1978, vol. 49, pp. 109–114.
- ³³ T. W. Miller, J. Jimenez, A. Sharan and D. A. Goldstein: "Oxygen Steel Making Process", in: R. J. Fruehan (ed.), *The Making, Shaping and Treatment of Steels: Steelmaking and Refining*, Volume 2. The AISE Steel Foundation, Pittsburgh, PA, USA, 1998, pp. 475–524.
- ³⁴ C. Cicutti, M. Valdez, T. Pérez, J. Petroni, A. Gómez, R. Donayo and L. Ferro: "Study of Slag-Metal Reactions in an LD-LBE Converter", *Proceedings of the Sixth International Conference on Molten Slags, Fluxes and Salts*, Stockholm-Helsinki, 2000.
- ³⁵ C. Cicutti, M. Valdez, T. Pérez, R. Donayo and J. Petroni: *Latin Am. Appl. Res.*, 2002, vol. 32, pp. 237–240.

-
- ³⁶ H. Jalkanen: “Experiences in Physicochemical Modelling of Oxygen Converter Process (BOF)”, in F. Kongoli and R. G. Reddy (eds.), *Advanced Processing of Metals and Materials (Sohn International Symposium), Volume 2, Thermo and Physicochemical Principles: Iron and Steel Making*, 2006, pp. 541–554.
- ³⁷ H. Jalkanen and L. Holappa: “Converter Steelmaking”, in: S. Seetharaman, A. McLean, R. Guthrie and S. Sridhar (eds.), *Treatise on Process Metallurgy*, 2014, vol. 3, Elsevier, Oxford, United Kingdom, pp. 223–270.
- ³⁸ M. Järvinen, V.-V. Visuri, E.-P. Heikkinen, A. Kärnä, P. Sulasalmi, C. De Blasio and T. Fabritius: *ISIJ Int.*, 2016, vol. 56, pp. 1543–1552.
- ³⁹ M. Ersson, L. Höglund, A. Tilliander, L. Jonsson and P. Jönsson: *ISIJ Int.*, 2008, vol. 48, pp. 147–153.
- ⁴⁰ M. Ek, Q. F. Shu, J. van Boggelen and D. Sichen: *Ironmaking Steelmaking*, 2012, vol. 39, pp. 77–84.
- ⁴¹ A. Kruskopf: *Metall. Mater. Trans. B*, 2015, vol. 46, pp. 1195–1206.
- ⁴² A. Kruskopf and S. Louhenkilpi, *Proceedings of the METEC & 2nd ESTAD*, Düsseldorf, Germany, 2015, p. 165.
- ⁴³ A. Kruskopf: *Metall. Mater. Trans. B*, 2017, vol. 48, pp. 619–631.
- ⁴⁴ M. H. A. Piro, Doctoral thesis, 2011, Royal Military College of Canada.
- ⁴⁵ M. H. A. Piro, S. Simunovic, T. M. Besmann, B.J. Lewis and W.T. Thompson, *Comput. Mater. Sci.*, 2013, vol. 67, pp. 266–272.
- ⁴⁶ M. H. A. Piro and S. Simunovic, *CALPHAD*, 2012, vol. 39, pp. 104–110.
- ⁴⁷ A.D. Pelton and C. W. Bale, *Metall. Mater. Trans. A*, 1985, vol. 17, pp. 1211–1215.
- ⁴⁸ G.K. Sigworth and J.F. Elliot, *Metal Sci.*, 1973, vol. 8, pp. 298–310.
- ⁴⁹ J. Miettinen, IAD – Thermodynamic Database for Iron-based alloys, Casim Consulting Oy, 2017, Espoo, Finland.
- ⁵⁰ A. D. Pelton and M. Blander, *Metall. Trans. B.*, 1986, vol. 17, pp. 805–815.
- ⁵¹ C. R. Swaminathan and V. R. Voller: *Int. J. Num. Meth. Heat Fluid Flow*, 1993, vol. 3, pp. 233–244.
- ⁵² J. R. Taylor and A. T. Dinsdale, *CAPHAD*, 1990, vol. 14, pp. 71–88
- ⁵³ HSC Chemistry 8, version 8.1.0, Outotec Technologies, 1974–2015.
- ⁵⁴ M. Timucin and A.E. Morris, *Metall. Trans.*, 1970, vol. 1, pp. 3193–3201.
- ⁵⁵ Slag Atlas, 1981, Verlag Stahleisen M.B.H., Düsseldorf, Germany, pp. 68.
- ⁵⁶ C. Cicutti, M. Valdez, T. Pérez, J. Petroni, A. Gómez, R. Donayo and L. Ferro, “Study of Slag-Metal Reactions in an LD-LBE Converter”, *Proceedings of the Sixth International Conference on Molten Slags, Fluxes and Salts*, Stockholm-Helsinki, 2000
- ⁵⁷ P. V. Riboud and M. Olette, “Mechanisms of some of the reactions involved in secondary refining”, *Proceedings of the 7th International Conference on Vacuum Metallurgy*, 1982, pp. 879–889. Iron and Steel Institute of Japan, Tokyo, Japan.
- ⁵⁸ S. Paul and D. N. Ghosh, *Metall. Trans. B*, vol. 17, pp. 461–469.
- ⁵⁹ M. Hirasawa, K. Mori, M. Sano, A. Hatanaka, Y. Shimatani and Y. Okazaki, *Trans. Iron Steel Inst. Jpn*, 1987, vol. 27, pp. 277–282.
- ⁶⁰ A. Chatterjee, N.-O. Lindfors and J.Å. Wester, *Ironmaking Steelmaking*, vol. 3, pp. 21–32.
- ⁶¹ K. Krishnapisharody and G.A. Irons, *Metall. Mater. Trans. B*, 2013, vol. 44, pp. 1486–1498.
- ⁶² A. Kärnä, M. P. Järvinen and F. Fabritius, *Steel Res. Int.*, 2013, vol. 86, pp. 1370–1378.
- ⁶³ S. Ban-Ya, *ISIJ Int.*, 1993, vol. 33, pp. 2–11.

List of table captions

Table 1. Linear parameters A and B of the molar first-order interaction parameters for the UIP activity model.

Table 2. Heat capacity functions for compounds ⁵².

Table 3. Model parameters.

Table 4. Comparison of the predicted carbon contents.

List of figure captions

Fig. 1. Algorithms for time integration and for minimizing Gibbs energy

**Fig. 2. Calculated iso-activity lines (solid green) compared with measurements (dashed black).
a) FeO activities, b) SiO₂ activities**

Fig. 3. Calculated liquidus lines for CaSiO₃ (solid cyan) and SiO₂ (solid green) compounds at three temperatures ($T = 1300^{\circ}\text{C}$ (1573 K), 1400°C (1673 K), 1500°C (1773 K)) compared with measurements (dashed black). Calculated liquidus lines for CaO(s) (yellow) and Ca₂SiO₄(s) (red) at temperature $T = 1900^{\circ}\text{C}$ (2173 K) compared with assumed liquidus lines (dashed black).

Fig. 4. Carbon and silicon concentrations in bulk metal as a function of time.

Fig. 5. Bulk slag composition as a function of time.

Fig. 6. The bulk metal and reaction zone temperatures as a function of time.

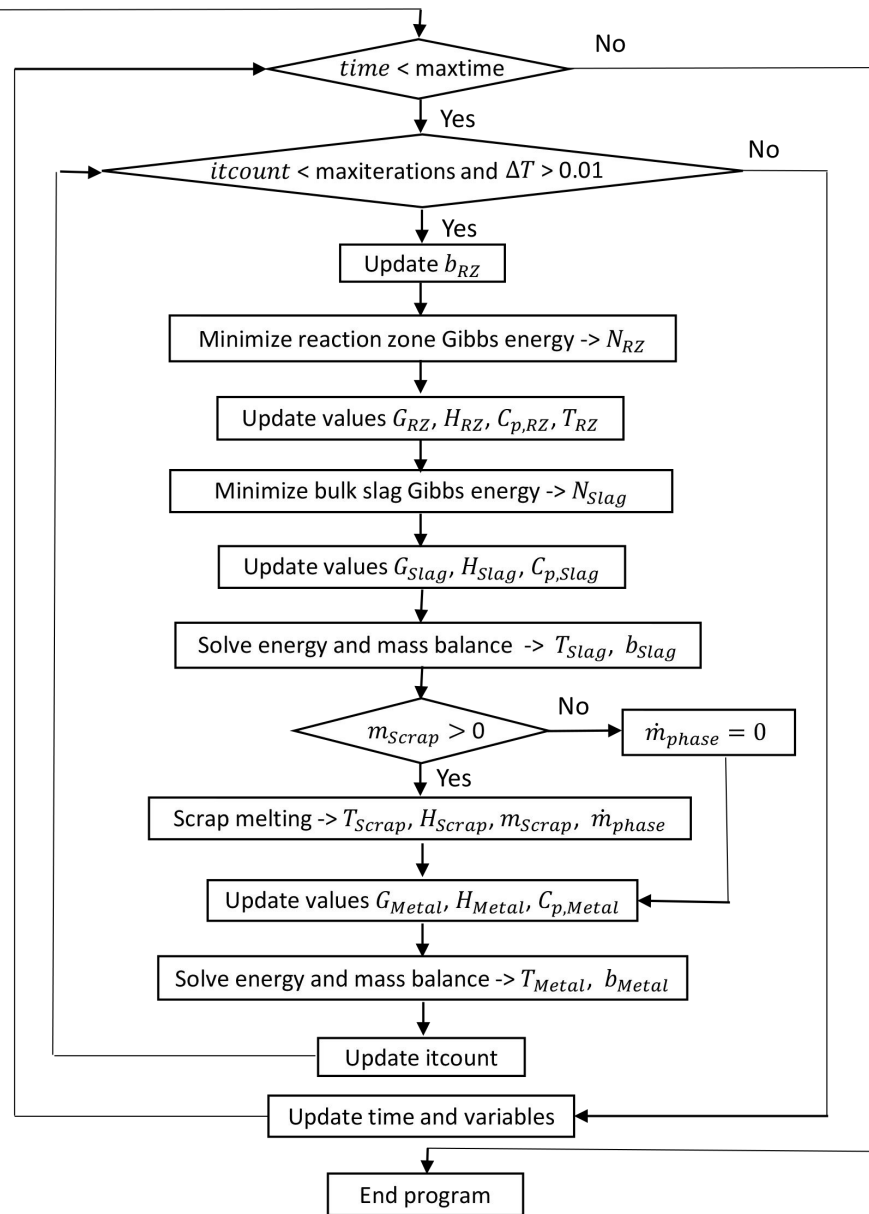
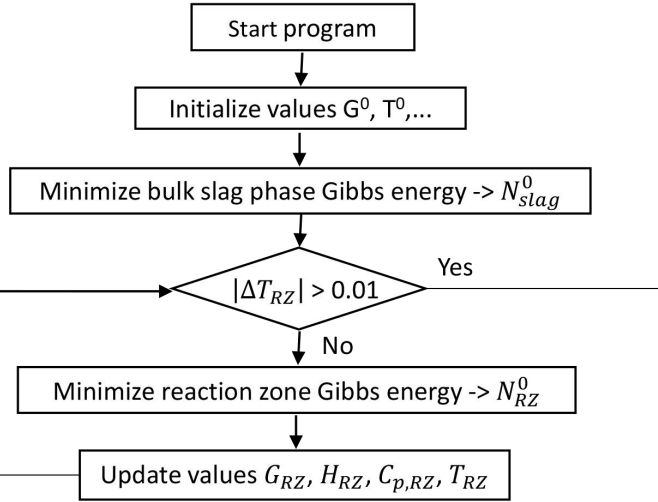
Fig. 7. Bulk slag solid mole fraction as a function of time a) and the amount of two solid components b).

Fig. 8. Comparison of the slag composition (a,b,c) and comparison of the carbon content in iron in fig. d with literature.

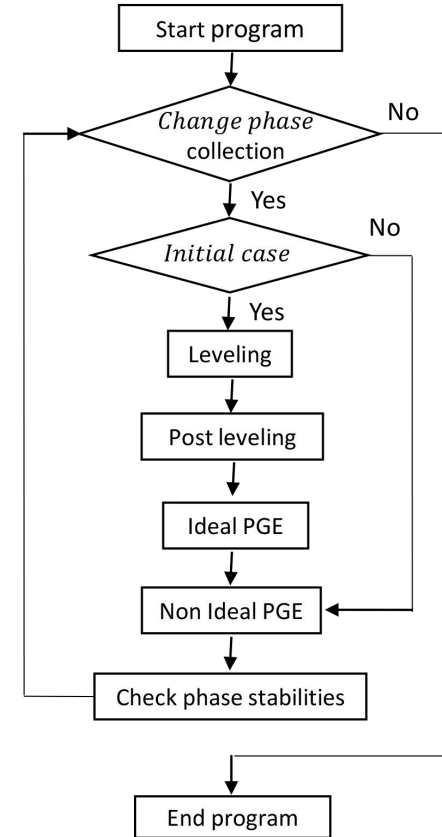
Fig. 9. Comparison of the implicit and explicit Euler algorithm with $dt = 1$ s and $dt = 5$ s. a) Comparison for carbon concentration in metal phase. b) Comparison for component concentrations in slag phase.

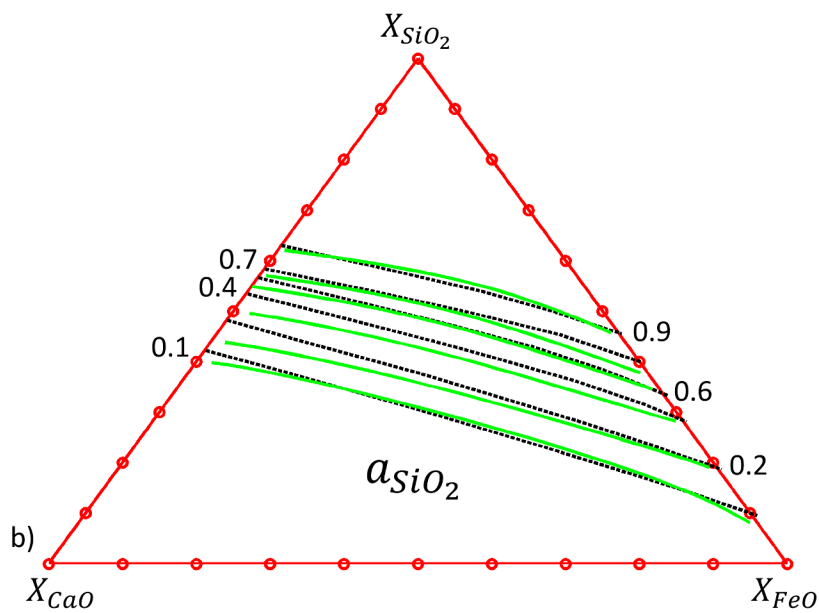
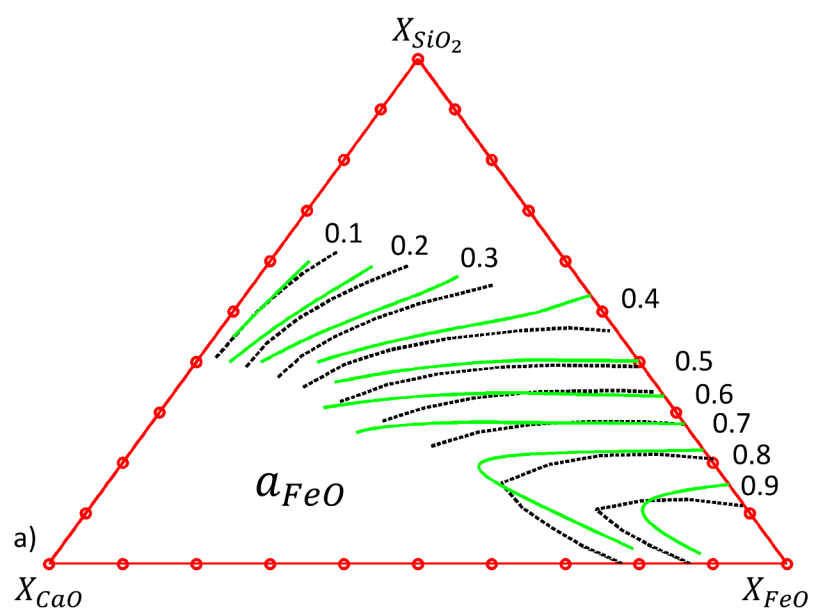
Fig. 10. All possible parabolas from a) to f) for Eq. (72) that can give limiting values for pair fraction.

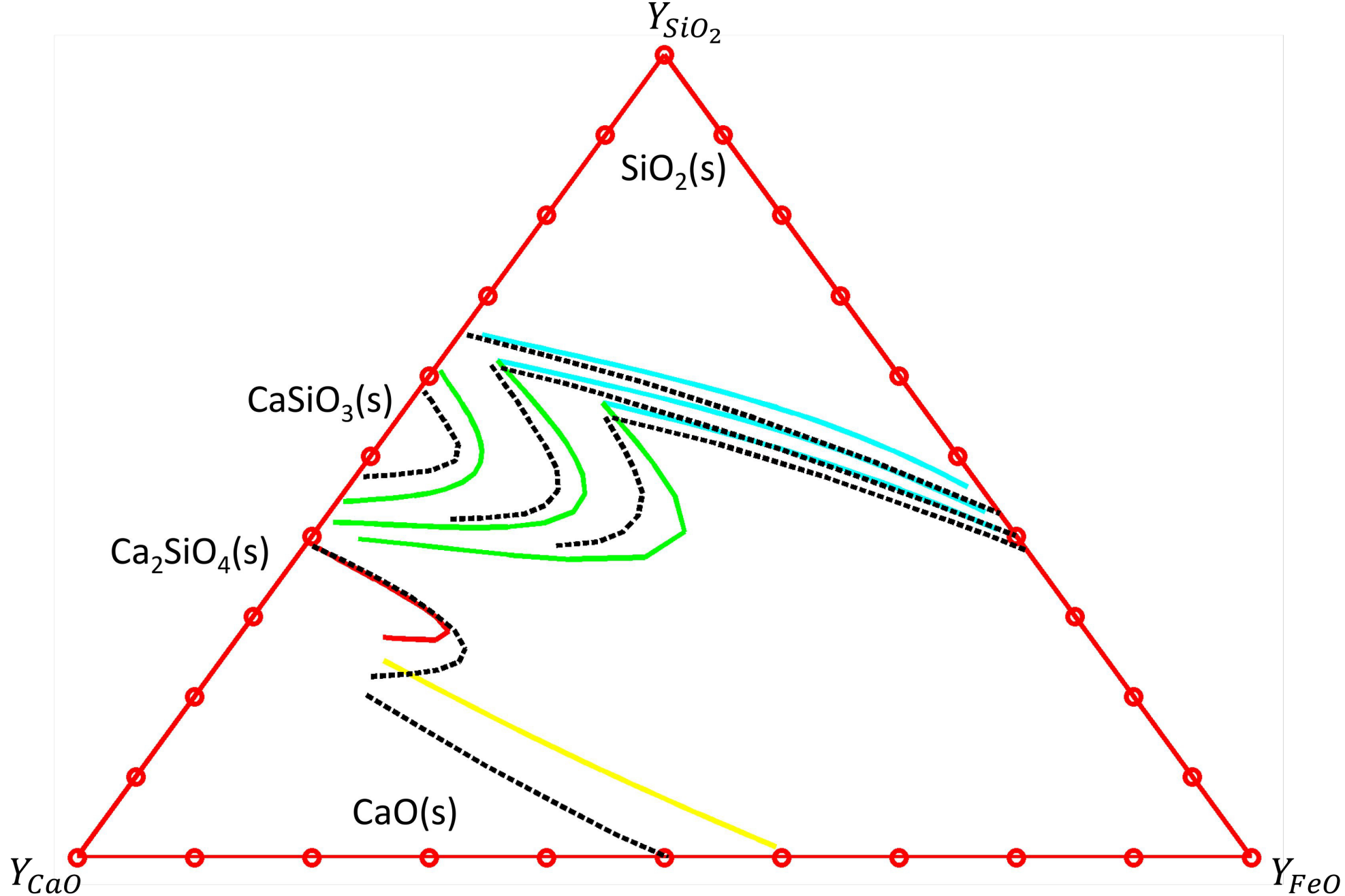
Algorithm 1: Time integration

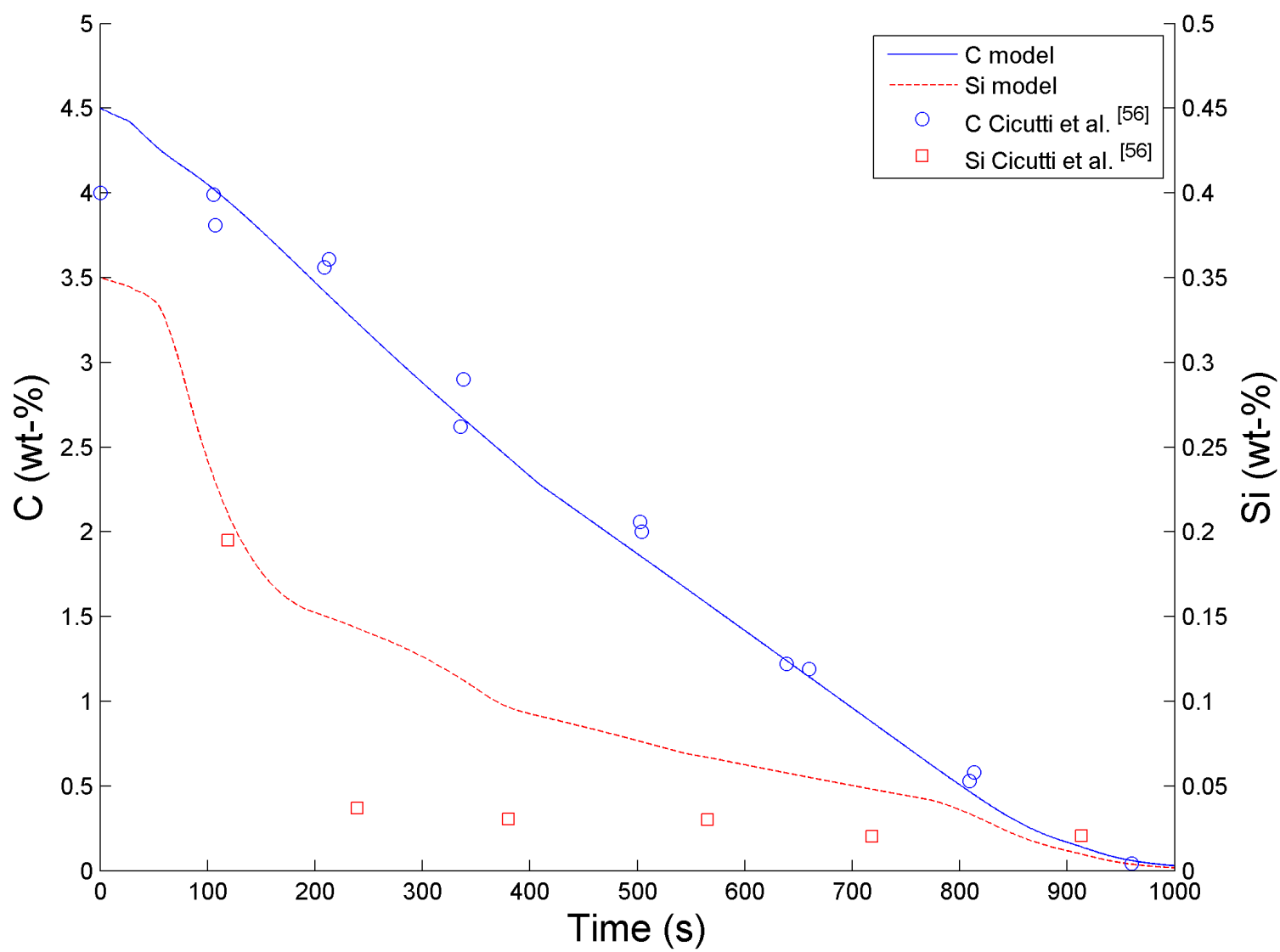


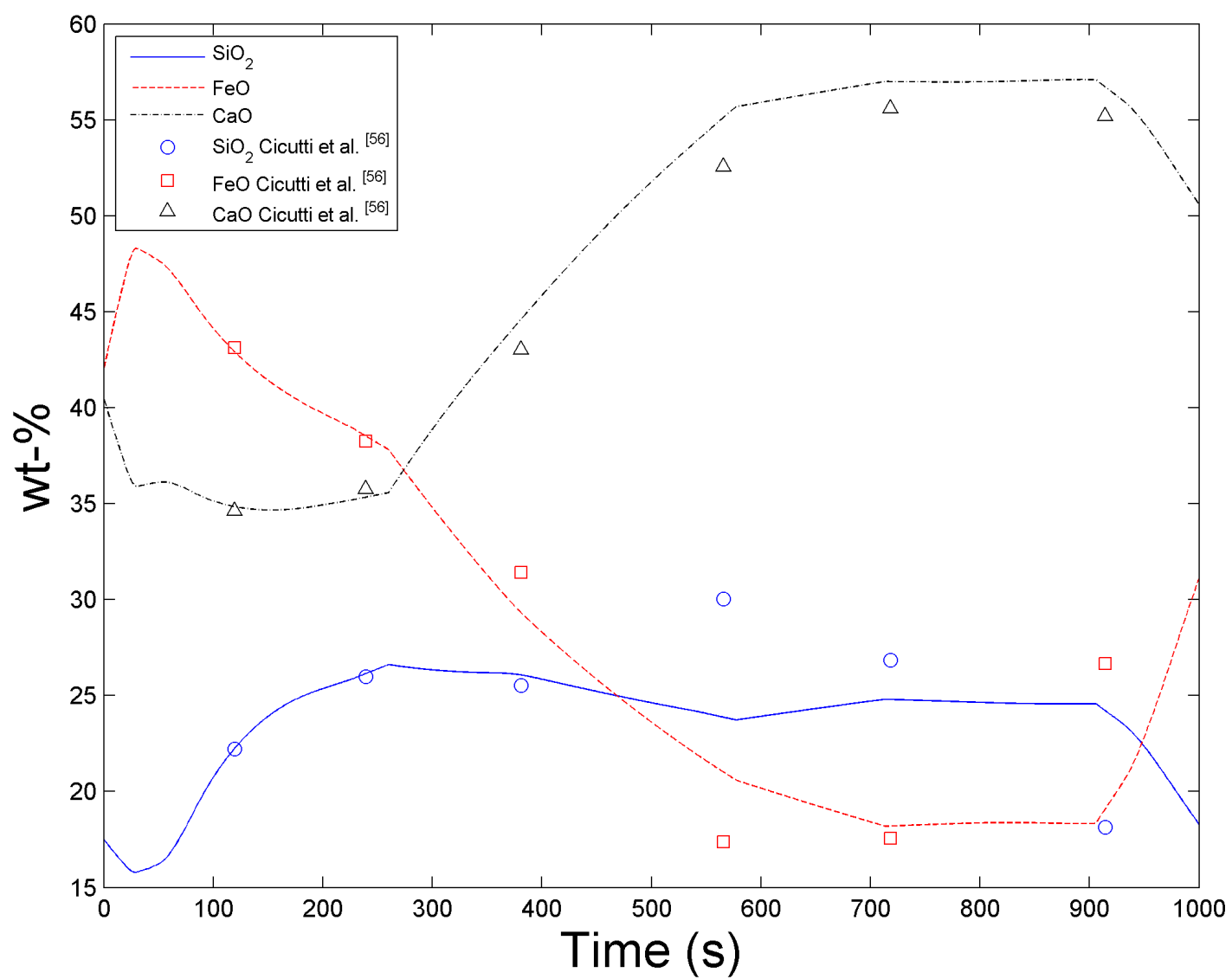
Algorithm 2: Gibbs energy minimization

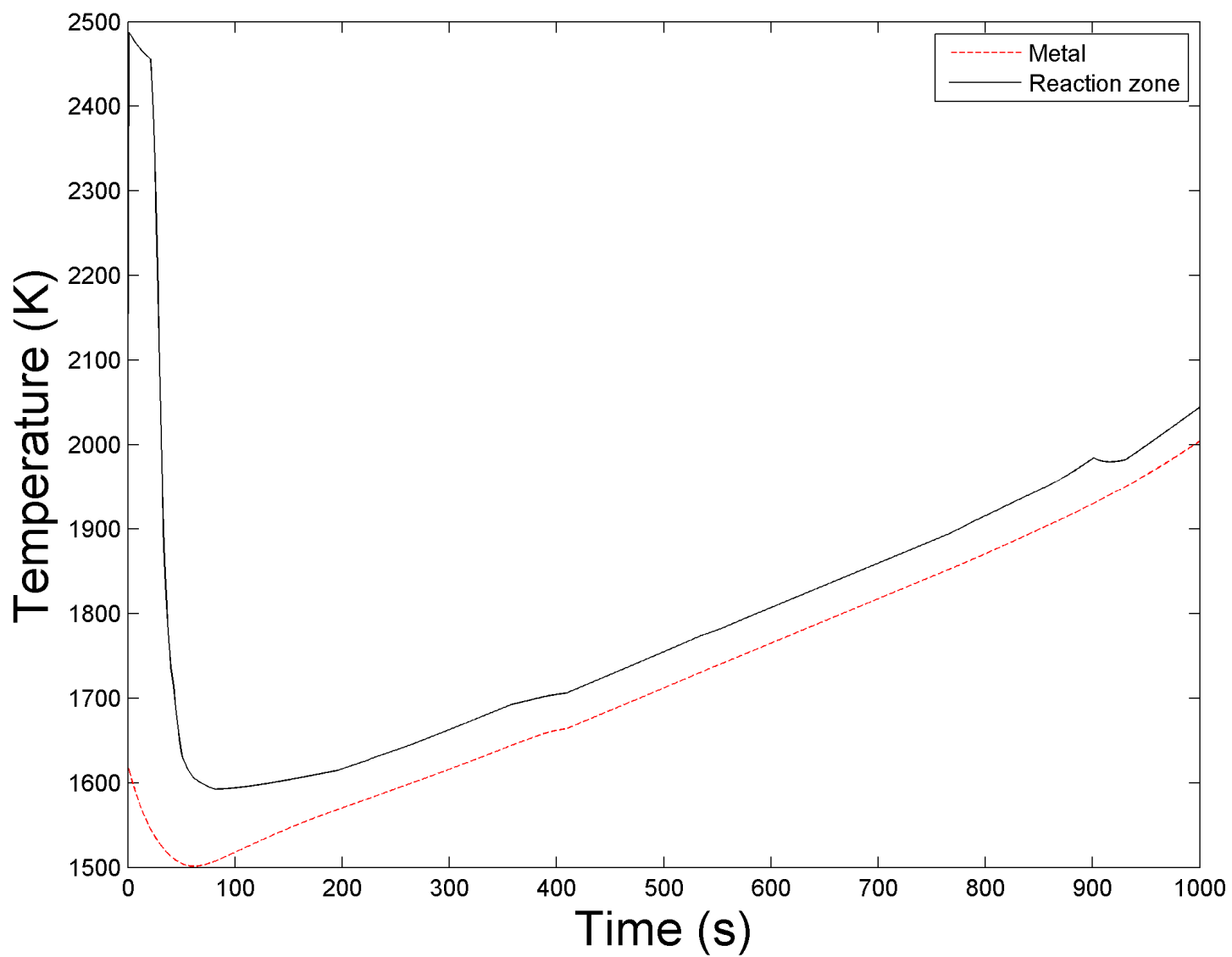


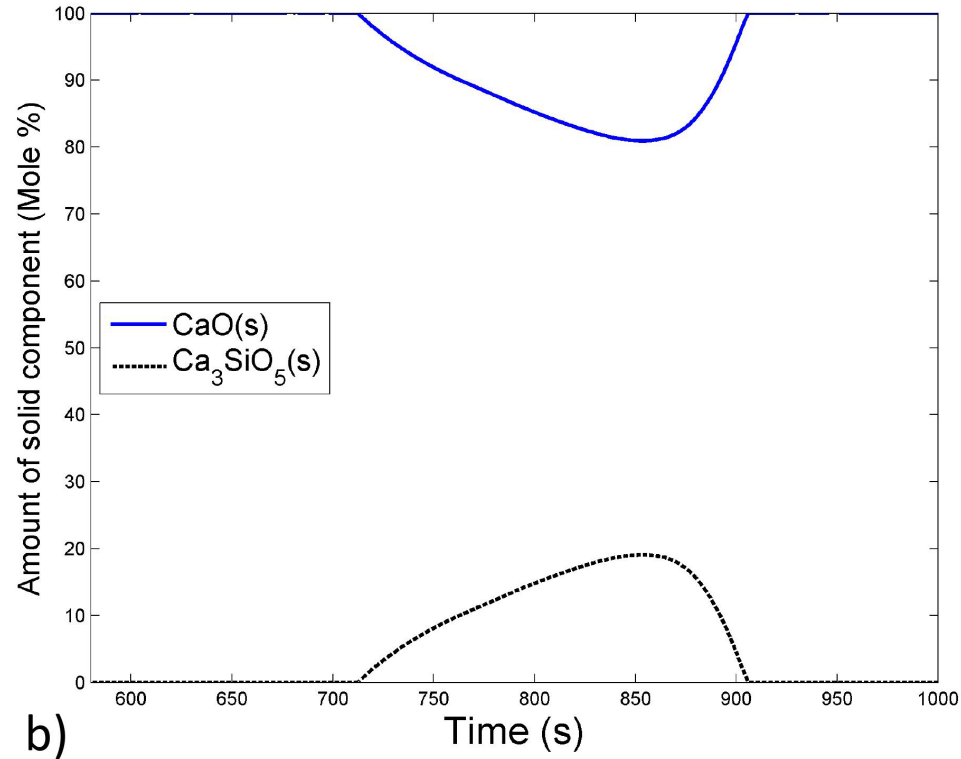
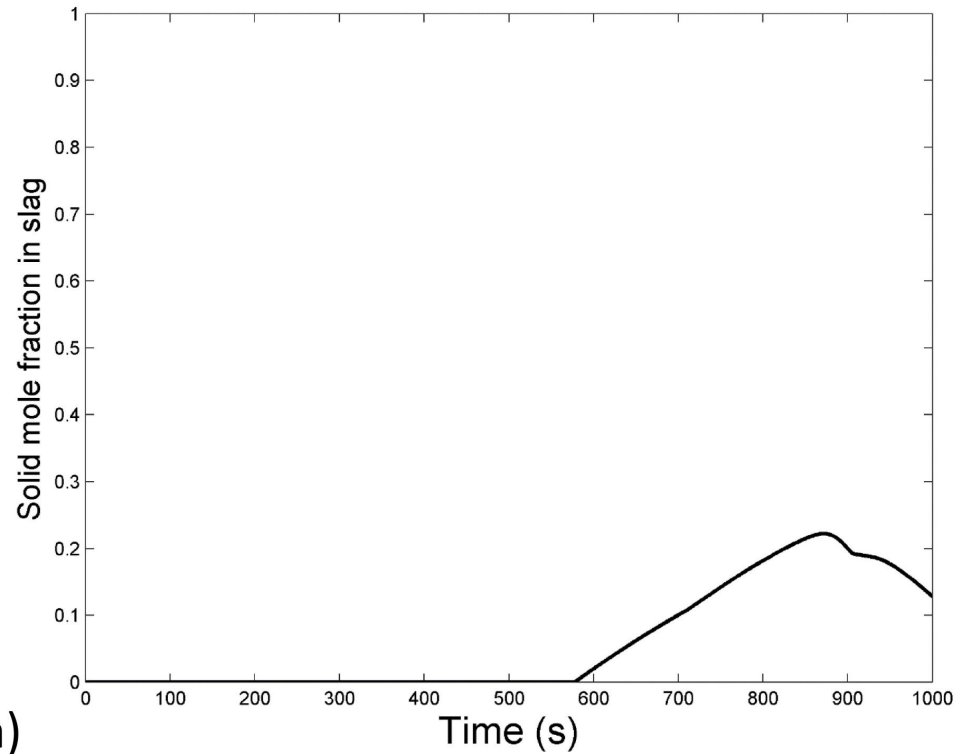


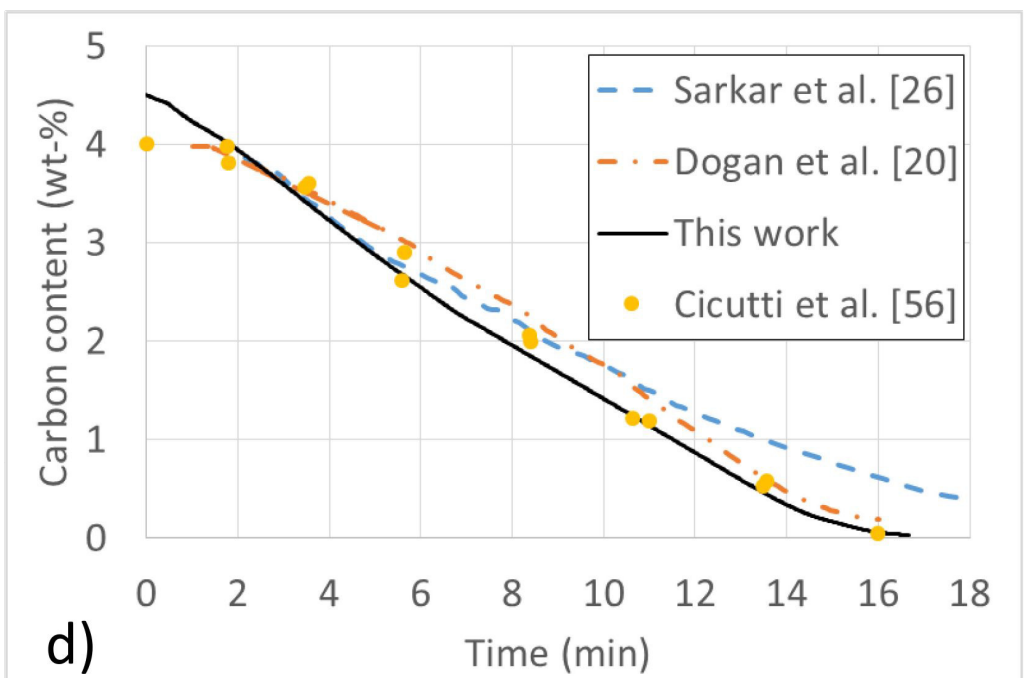
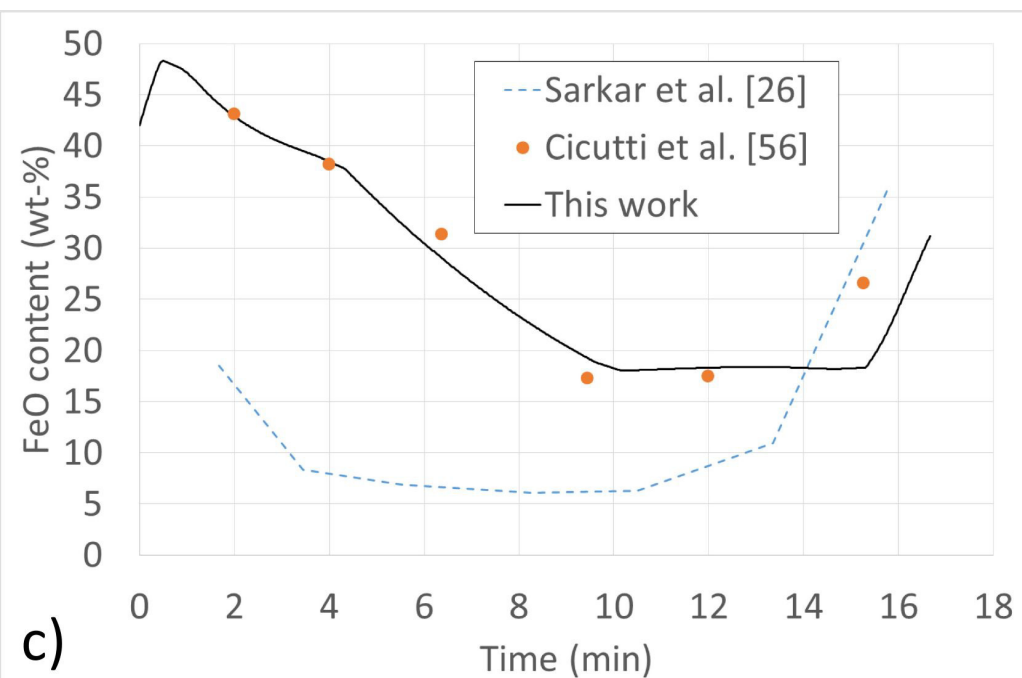
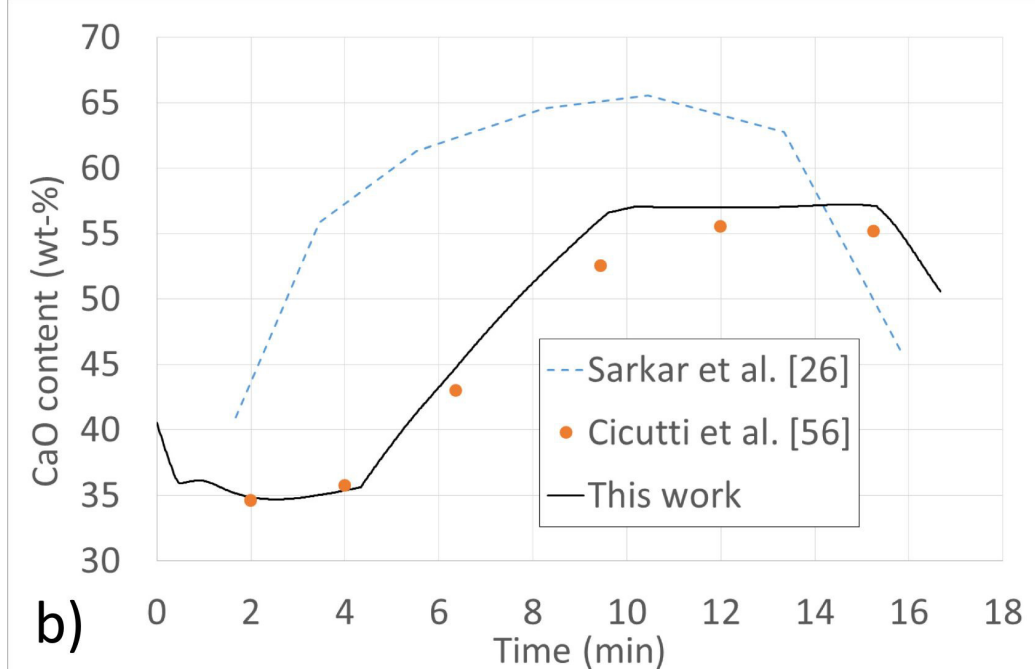
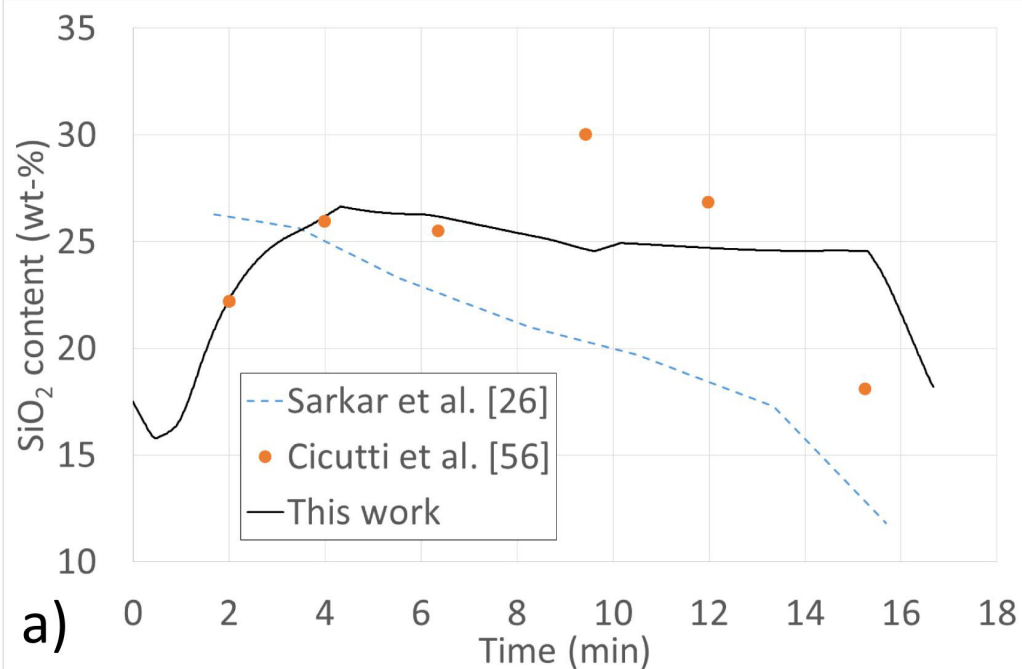




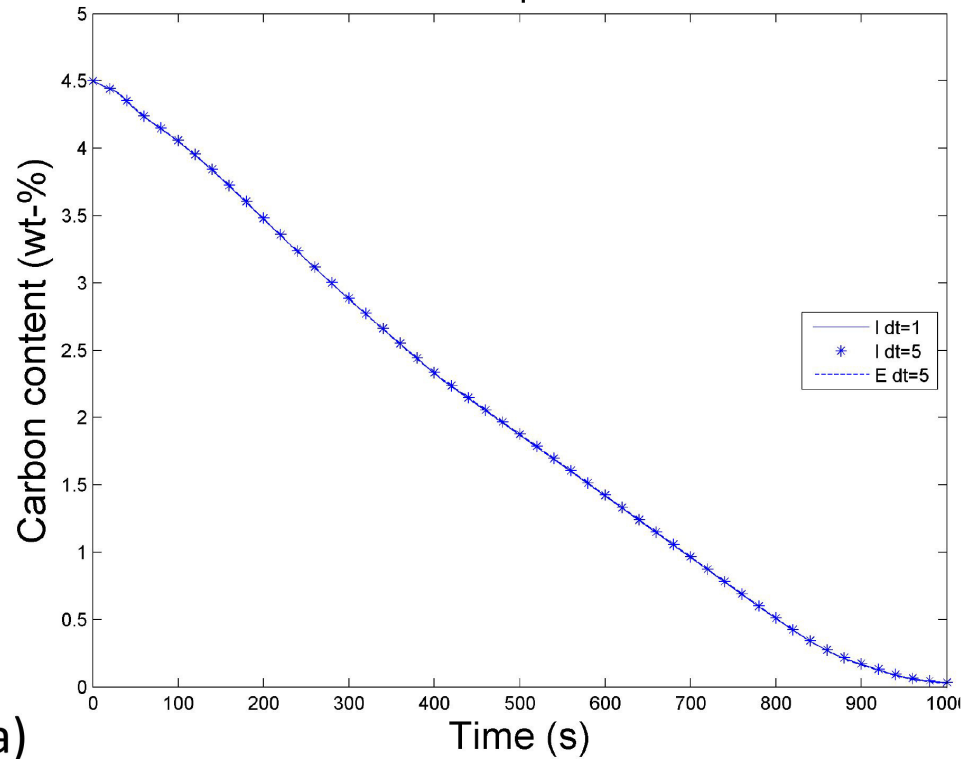






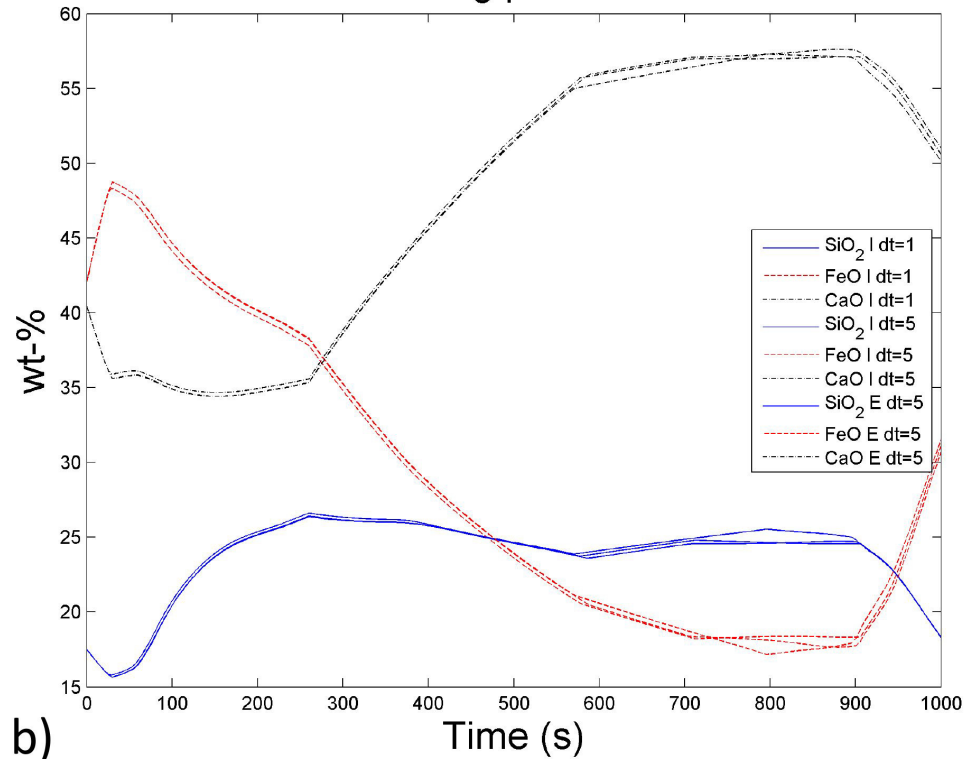


Metal phase



a)

Slag phase



b)

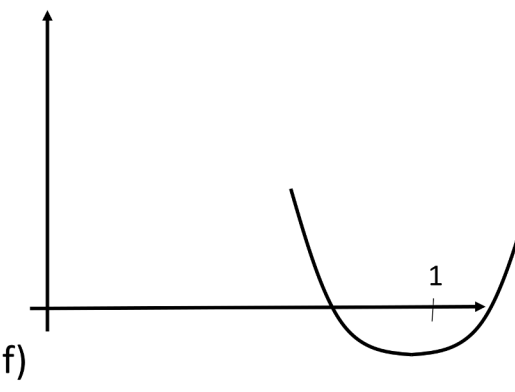
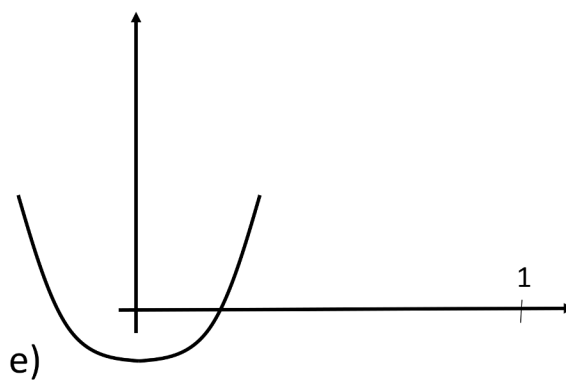
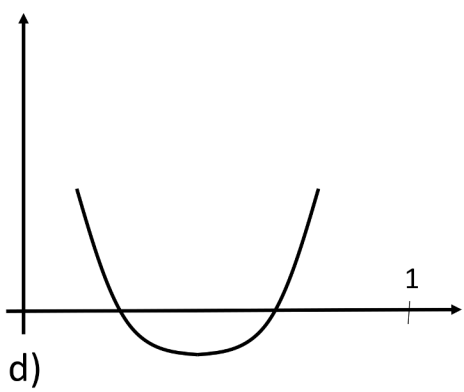
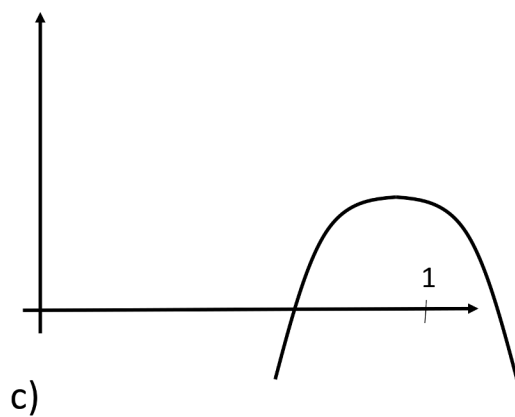
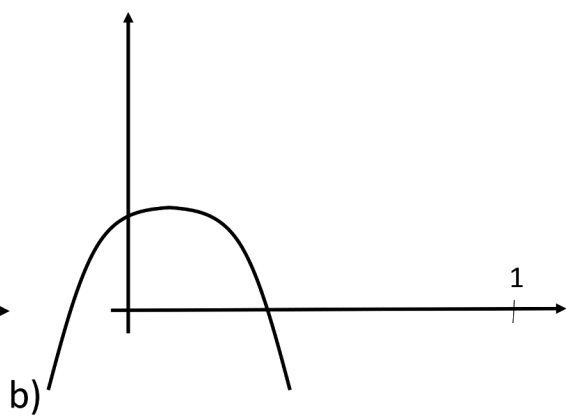
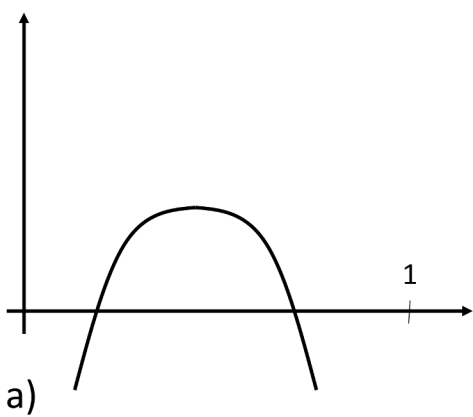


Table 1. Linear parameters A and B of the molar first-order interaction parameters for the UIP activity model.

A	C	O	Si		B (K)	C	O	Si
C	3.66	-21.7	-0.429		C	7824	0	18760
O	-21.7	100	-14.7		O	0	-115400	0
Si	-0.429	-14.7	10.8		Si	18760	0	3996

Table 2. Heat capacity functions for compounds⁵².

	$C_p(T) = A \cdot 10^5 T^{-2} + B + C \cdot 10^{-3} T + D 10^{-6} T^2$				T_1	T_2	H_{tr}	S_{tr}
	A	B	C	D	K	K	kJ/mol	J/(mol · K)
SiO ₂ (l)	-13.3110	52.1700	24.0040	-4.0680	298.15	2980		
SiO ₂ (s)	262.88	-1399.89	5715.82	-6244.89	298.15	373	-908.137	43.065
	-582.0055	2178.36	-6987.2180	6457.28	373	453		
	-2550.05	7860.21	-23634.30	20191.10	453	543		
	-44.5425	77.5875	-6.0805	2.7787	543	3300		
		87.3730			3300	4000		
CaO(s)	-9.3661	51.8583	2.4386	0.0001	298.15	3172	-634.92	38.1
CaSiO ₃ (s)	-13.6411	80.2293	83.7141	-38.55	298.15	800	-1634.6	81.479
	-51.2087	117.28	18.0493	-5.2147	800	1398.15		
	-40.2891	113.25	12.0608	-1.9948	1398.15	3500	1.736	1.24164
Ca ₂ SiO ₄ (s)	-8.9137	100.48	133.78	-51.515	298.15	950	-2317.38	120.499
	21.5445	71.2369	183.5875	-75.2890	950	1120		
	-0.0003	161.53	-0.0010	18.9499	1120	1710	14.162	12.6446
		173.68	0.8873		1710	3500	14.386	8.41287
Ca ₃ SiO ₅ (s)	-23.9027	161.3170	142.3400	-59.15	298.15	850	-2933.21	168.604
	-91.4586	224.09	35.3570	-7.2380	850	1550		
		226.5211	20.1100		1550	3500		
Ca ₃ Si ₂ O ₇ (s)	-31.0041	198.4530	188.2052	-92.0488	298.15	800	-3954.05	210.543
	-115.6638	283.2210	35.1320	-12.4937	800	1650		
		296.1880	4.0814		1650	3500		

Table 3. Model parameters.

	mass (kg)	T (K, °C)		
Hot metal	170000	1623 (1350)		
Slag	6500	1623 (1350)		
Scrap	30000	300 (27)		
Oxygen mass flow		12	kg/s	
Argon gas flow rate		150-500	m ³ /h NTP	
time step		1	s	
Scrap heat transfer coeff h_T		20000	W/(m ² *K)	
Scrap carbon mass transfer coeff h_Y		0.0002	m/s	
Scrap thickness		3.0	cm	
Scrap Area		286	m ²	
<u>Composition</u> (wt-%)		C	Si	
hot metal		4.5	0.35	
scrap		0.25	0.1	
		FeO	SiO ₂	CaO
slag		42	17.5	40.5

Table 4. Comparison of the predicted carbon contents.

Time [min]	Carbon content [wt-%]			
	Measured	This work	Sarkar <i>et al.</i> ²⁶	Dogan <i>et al.</i> ²⁰
1.8	3.90	4.02	3.88	
3.5	3.59	3.41	3.54	3.43
5.6	2.76	2.68	3.03	2.76
8.4	2.03	1.86	2.24	2.09
10.6	1.22	1.25	1.53	1.34
11.0	1.19	1.15	1.42	1.50
13.5	0.55	0.46	0.62	1.00
16.0	0.04	0.06	0.19	0.62
MAE [wt-%]	—	0.09	0.16	0.24
RMSE [wt-%]	—	0.11	0.19	0.31